POLITECNICO DI TORINO

Master of Science in Aerospace Engineering

Master's Degree Thesis

INVESTIGATION OF CAPILLARY - DOMINATED FLOWS: EXPERIMENTAL AND NUMERICAL ANALYSIS

Supervisors:

Prof. Dario Giuseppe Pastrone

Prof. Miguel Alfonso Mendez

Dr. Alessia Simonini

Domenico Fiorini

Candidate:

Francesco Federico s281723

Academic Year 2022/2023

Abstract

This thesis concerns the characterization and modeling of the wetting dynamics of capillary-dominated flows.

The objectives of this research are twofold: to improve the understanding of the wetting behavior of cryogenic propellants and to establish an extensive database encompassing various conditions and geometries for the validation of predictive models. Both objectives play a pivotal role in the management of space propellants in a gravity-free environment. We investigate experimentally the wetting dynamics of cryogenic model fluids using a quasi-capillary U-tube where oscillations of a liquid column are induced in response to a pressure step imposed on one of the two sides. The experiments record the gas-liquid interface motion and deformation using high-speed cameras and backlight configuration. Several fluids have been investigated, covering a wide range of viscosity and surface tension combinations. We focused most of our attention on HFE7000 and HFE7200, used as model fluids for space propellants. The comparison of the experiments shows considerable differences in wetting behavior. In tests with HFEs, it is observed that deformations at the gas-liquid interface can be divided into two regimes: one dominated by gravity and the other by inertia. In the first regime, small, wetting-dependent deformations are observed. On the other hand, in the inertial-regime the interface assumes a wider range of shapes, varying with the instantaneous acceleration. These same behaviors do not emerge in tests with demineralized water. In this case, the seemingly random occurrence of the stick-slip phenomenon introduces rapid changes from concave to convex shapes and, consequently, produces largely different dynamics of the interface deformations.

Finally, we used Computational Fluid dynamics (CFD) and Volume of Fluid (VoF) method without interface reconstruction to simulate the experimental test cases and investigate the accuracy of the numerical wetting models. The comparison between the simulations and the experiments shows that capillary effects are still inadequately modeled in CFD solvers, where only fluid hydrodynamics is considered.

Contents

List of Figures

List of Tables

Chapter 1

Introduction

In the field of fluid dynamics, a topic of great relevance concerns capillary flows, or more generally, flows in which capillary forces predominate over the other forces at play.

These flows occur for example in a gravity-free environment such as in space during the utilization of liquid propulsion systems or for the general management of fluids on spacecraft. In this case, due to the absence of gravity, the fluids are accelerated mainly by surface tension forces occurring at the gas-liquid interfaces.

On the ground, other examples of capillary-driven flows concern the imbibition of porous media [1], capillary flows in microfluidics [2], and surface coating (e.g. Slot-die coating [3]). The study of these flows is critical for various engineering applications, including microfluidic for biomedical applications [4]. For instance, as depicted in Fig. 1.1, can be observed the self-driven, contactless manipulation of a solvent.

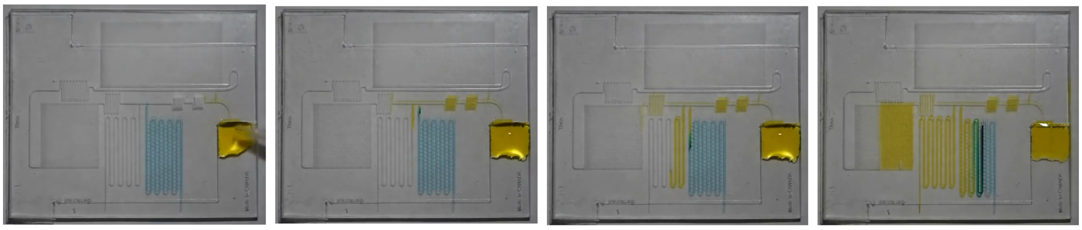

Figure 1.1: Capillary Driven Microfluidic for one Step Immunoassay *(credit to Sensoreal)*

Capillary-driven systems play a central role in the design of cooling systems for electronics, where capillarity is used to enhance cooling efficiency [5]. On a larger scale, capillary phenomena are also explored for their significance in controlling and managing water resources within civil and environmental engineering [6].

In this work, we focus on the management of fluids in microgravity conditions.

Typical applications in aerospace are the design and optimization of power systems, cooling systems, tanks, thrusters, and life support devices [7].

In the context of liquid propulsion in low-gravity environments, it is crucial to anticipate the propellant's motion within the propellant tank [8]. To comprehend propellant dynamics, one must ascertain its location and movements within the tank and have the capability to forecast its actions throughout the mission. Sloshing is a phenomenon that occurs when the free interface between liquid and gas inside a container begins to move in response to external forces. In the space environment, this phenomenon occurs inside tanks that contain a significant amount of fuel used for trajectory maneuvers. As the fuel is consumed, the level in the tank changes, and the fuel begins to move in accordance with the accelerations and movement of the spacecraft. The forces generated by this movement can affect the accuracy of spacecraft maneuvers, making it crucial to predict the effect of sloshing on the control system [9]. On the other hand, the accurate prediction of the sloshing motion in micro-gravity conditions poses considerable challenges. While gravity dominates the fluid motion and acceleration on the ground, in microgravity capillary forces change drastically the balance and induce unfamiliar flow behaviors.

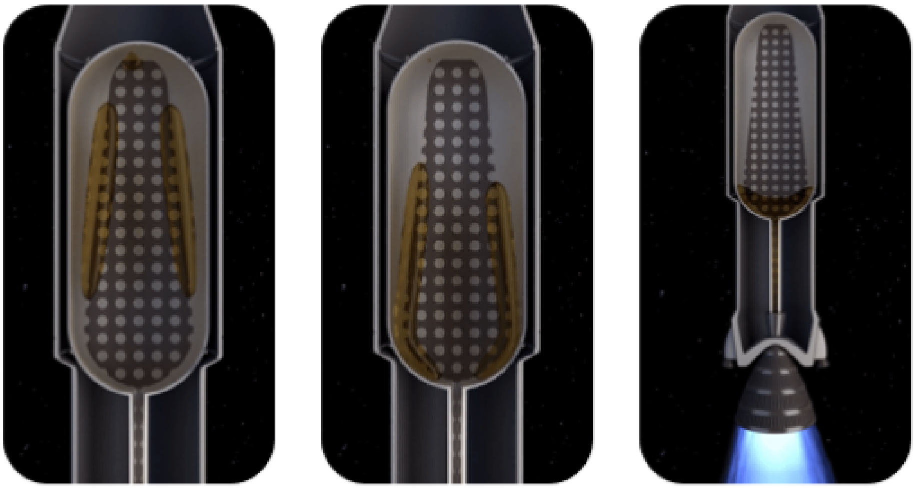

Figure 1.2: Propellant delivery to engine *(credit to NASA Johnson)*

Propellant Management Devices, shown in Fig. 1.2, is an example where capillary flow plays a key role. It concerns the efficient transfer of liquid propellants from tanks to spacecraft engines, in zero-g conditions.

In microgravity, the surface tension of the propellant becomes the predominant factor affecting the distribution inside the tank. The liquid tends to wet all the surfaces, leaving a gaseous core inside. For this reason, Propellant Management Devices (PMDs) may be required inside the tank [10]. As shown in Fig.1.3, on the ground or during the launch phase, when thrust and a high-g environment coexist, PMDs are not required, the fluid can safely feed the engine. When low-gravity environments are reached, Liquid Acquisition Devices must be used to prevent inadequate fluid supply to the engine. This system allows the engine to be constantly supplied with propellant, avoiding an inadequate feed of liquid and gas [11]. In all these capillarity applications, a key parameter describing the interaction between the liquid and the solid surfaces is the contact angle formed by the gas-liquid interfaces with the solid surface. This parameter models the ability of the liquid to wet the solid and move within a duct or on a surface, impacting the shape of gas-liquid interfaces and the dynamics of capillarity systems in free (or low) gravity environment [7]. Consequently, the accurate modeling of this parameter plays a central role in the prediction of fluid motion and the design of control systems for fluid management [12].

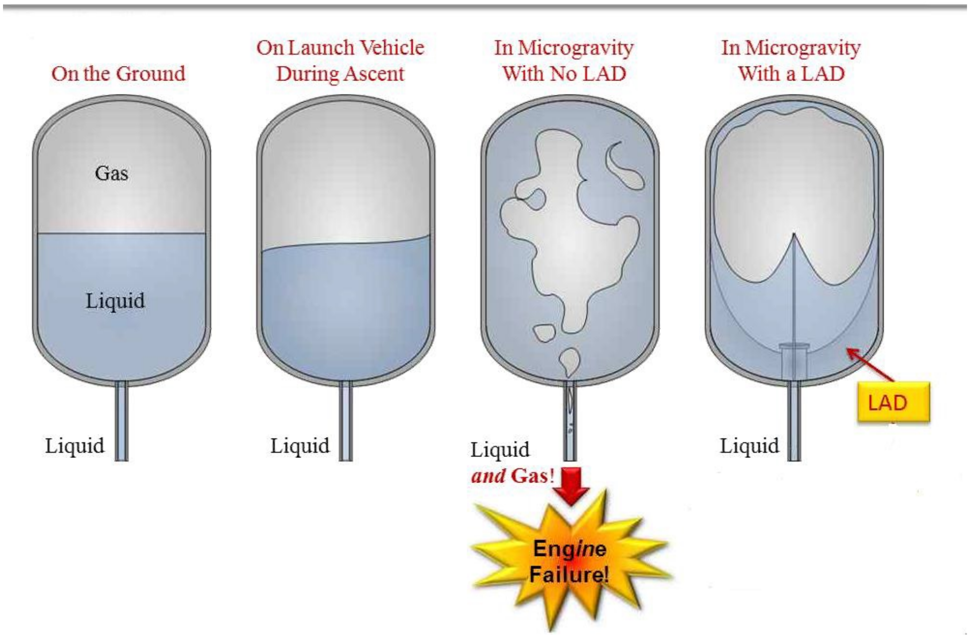

Figure 1.3: Why Liquid Acquisition Devices are required [11]

1.1 Contact angle

A crucial parameter to build a reliable model to predict the behavior of the capillary-driven flow is the **contact angle**. As shown in Fig 1.4, the static contact angle is the angle formed by the liquid-gas interface with the solid surface. It quantifies the capacity of

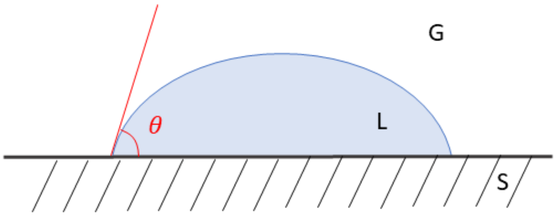

Figure 1.4: Contact angle

a solid to be wetted by a liquid. In static conditions, the liquid and the solid combination are characterized by Young's law:

$$\gamma_{SG} - \gamma_{SL} - \gamma_{LG} \ \cos\theta_s = 0$$

where:

- γ_{SG} is the solid–gas interfacial energy;
- γ_{SL} is the solid–liquid interfacial energy;
- γ_{LG} is the liquid–gas interfacial energy;
- θ_s is the static contact angle.

When a liquid is moving on a solid surface, it is possible to observe the so-called dynamic contact angle. Imagining a droplet for simplicity, Fig. 1.5, it is important to note two distinct angles: the advancing angle and the receding angle. The advancing angle θ_a is the angle formed between the solid surface and the drop as it expands, while the receding angle θ_r is the angle formed during the drop's retraction. The advancing angle tends to increase as the velocity of the liquid on the surface increases; conversely, the receding

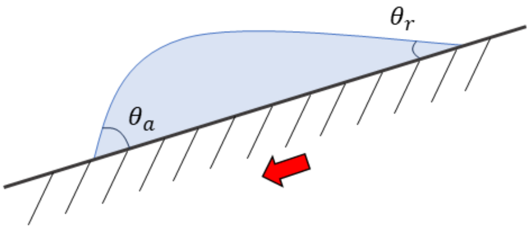

Figure 1.5: Advancing and receding contact angle

angle tends to decrease as the velocity increases [13].

When the liquid is in a stationary condition, the phenomenon of hysteresis, defined as the difference between advancing and receding contact angle, $\theta_a - \theta_r$, occurs.

Here are some various experimental methods for determining the contact angle.

The sessile drop method

One of the most common methods for measuring the static contact angle is the *sessile drop method*. It consists of placing a drop of the liquid to be tested on a solid surface and measuring the contact angle using image processing. There is a dynamic variant of this method that involves tilting the surface, for example. This new condition will show an advancing and a receding contact angle.

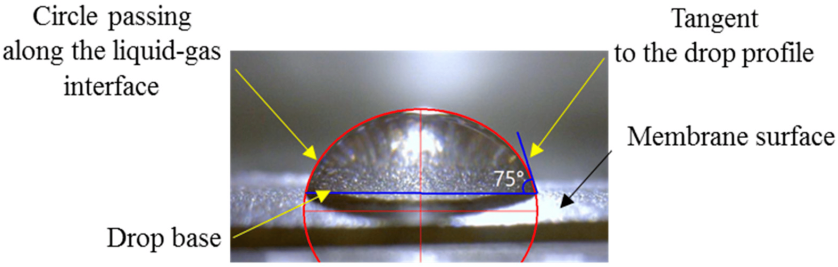

Figure 1.6: Sessile drop method *(credits to [14])*

The pendant drop method

The *pendant drop method* can be used to measure the contact angle of a drop by image processing. A drop of liquid to be tested is released from a needle; the shape of the drop depends on the balance of forces involved, including surface tension.

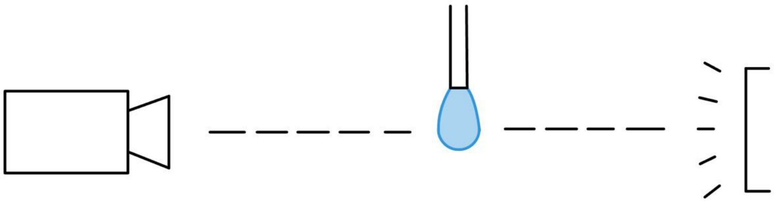

Figure 1.7: Pendant drop method

Dynamic Wilhelmy method

With the *Wilhelmy method*, it is possible to calculate the contact angle by immersing a thin surface in a liquid bath, which allows the advancing contact angle to be calculated, and bringing it to the surface, calculating the receding contact angle.

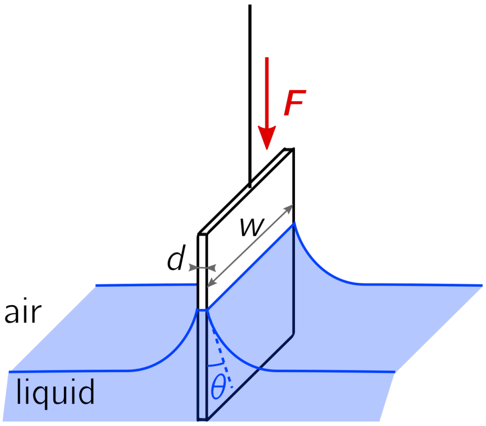

Figure 1.8: The Wilhelmy method *(credits to Wikipedia)*

The microscopic scale of the dynamic contact angle requires the use of appropriate optical instrumentation to clearly visualize the liquid-gas interface. Because of this difficulty in visualization, the results obtained may be subject to uncertainty, particularly near the solid surface, where the interface is approximately tangent to the wall and the point of contact becomes indistinguishable. Petrov and Sedev [15] consider the dynamic contact angle as not observable through optical means and attempt to overcome this limitation by using an approach known as the Meniscus Profile Method (MPM), which is based on an analytical formulation of the meniscus interface.

Modeling contact angle properties has an important role when simulating free-surface flows [16] using Computational Fluid Dynamics (CFD). In Propellant Management problems in Rocket Tanks, it is important to trace the three-dimensional behavior of liquid surfaces and contact line displacement in low gravity conditions. Since there are not many opportunities to test the microgravity, CFD plays a key role [17].

In flows involving two immiscible fluids in contact with a solid surface, the position of the contact line is of considerable interest. However, when attempting to simulate these flows using the Navier-Stokes equations numerically, a problem known as the contact line paradox arises [18]. This paradox stems from the fact that the Navier-Stokes equations require the fluid velocity to be zero at the solid surface (the 'no-slip' condition). But when the contact line moves, the fluid velocity must change abruptly from zero to a different value along the solid surface. This abrupt change in fluid velocity can lead to a numerical singularity, which means that the equations can produce physically unacceptable results as shown by Schönfeld and Hardt [16].

In this work, the dynamics of an accelerating meniscus with a quasi-capillary U-shaped tube geometry were analyzed. The research focused on investigating the interface dynamics of various liquids to give a comparative analysis. The primary emphasis was placed on examining the behavior of two specific liquids, namely HFE7000 and HFE7200 by 3M Novec.

To assess the wetting behavior, we employed two distinct techniques. Firstly, we measured the static contact angle using the MPM. Secondly, we determined the dynamic contact angle through the application of the Support Vector Regression (SVR) technique, appropriately analyzing the differences between the two methods.

In addition to experimental measurements, we conducted CFD simulations with the Volume of Fluid (VoF) method without interface reconstruction. Our objective in performing these simulations was to develop a robust and reliable, non-mesh-dependent model capable of predicting wetting phenomena accurately.

Chapter 2

Methodology

This study experimentally characterized the dynamics of an oscillating gas-liquid interface by using a U-shaped tube test case. This research seeks to extend the work conducted by Fiorini et al. [19] but using both HFE7200 and HFE7000 as primary working fluids. With a view to a comprehensive comparison, other fluids were also introduced to provide an analysis of their respective behaviors.

In this chapter, we will provide an overview of our experimental setup, detailing all the steps and precautions taken during the entire phase of the experimental campaign.

To capture the dynamics of the liquid-gas interface, we used a high-speed camera at a rate of 300 frames per second. We characterized the shape of the gas-liquid interface and its position using edge detection.

We next used two types of models for the interface regression. The first method is based on the Meniscus Profile Method, which consists of fitting the experimental interface data following a physical model, using the contact angle as an optimization parameter. The second approach involves the use of Support Vector Regression to fit the experimental data. In this case, the contact angle is obtained by calculating the wall tangent of the regression curve.

We conducted a series of tests to study the evaporation of HFEs, which have a high volatility. The aim of these tests was to understand how to address the saturation problem in our experimental system.

In addition to conducting the experimental tests, we also developed a CFD model to complement our experiments and gain a more complete and detailed understanding of the problem.

2.1 Facility description

For the experiments performed we used a wide range of liquids whose properties are shown in Table 2.1 at standard conditions, 25 °C and 1 *atm* [20].

		HFE7200	HFE7000	Dem. water	Isopropanol	Ethanol	Diprop. Glycol
Density (ρ)	kg/m^3	1423.00	1404	997	785	789	1020
Dynamic viscosity (μ)	$mPa\ s$	0.64	0.49	0.97	2.46	1.20	75.00
Surface tension (σ)	mN/m	13.62	12.33	72.01	21.70	22.39	35.00

Table 2.1: Fluid physical properties at 298 K

Experimentation focused on HFE7000 and HFE7200, used as similar fluids of space propellants.

The experiment was conducted using a PIERREGLASS (Belgium) quartz U-shaped tube. We tested two different dimensions of the tube: the first had an internal diameter of 8 mm and an axial length of 164 *mm*, while the second had an internal diameter of 7 mm and an axial length of 197.7 *mm*, both shown in Figures 2.1 and 2.2.

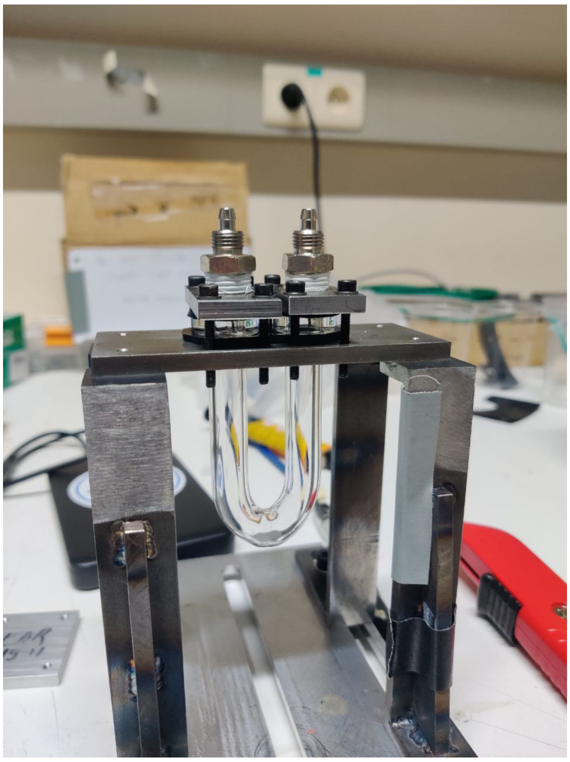

Figure 2.1: First Tube

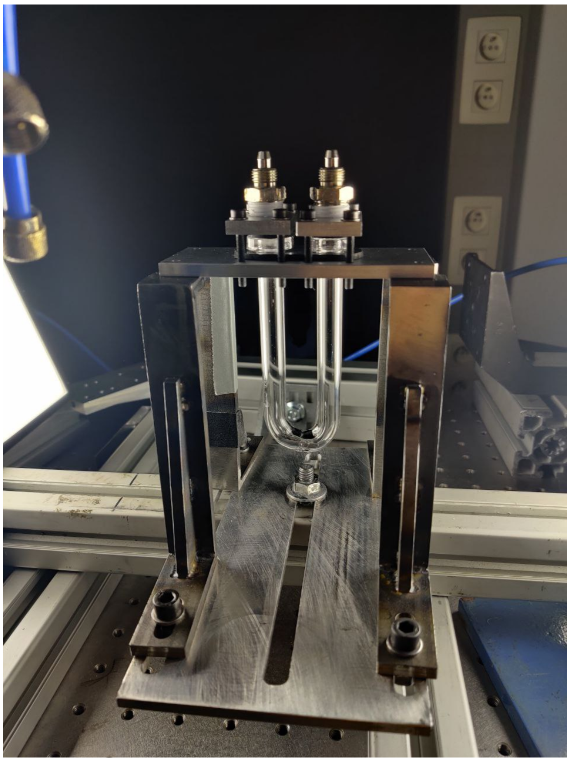

Figure 2.2: Second Tube

The experimental setup is shown in the pictures 2.4 and 2.5.

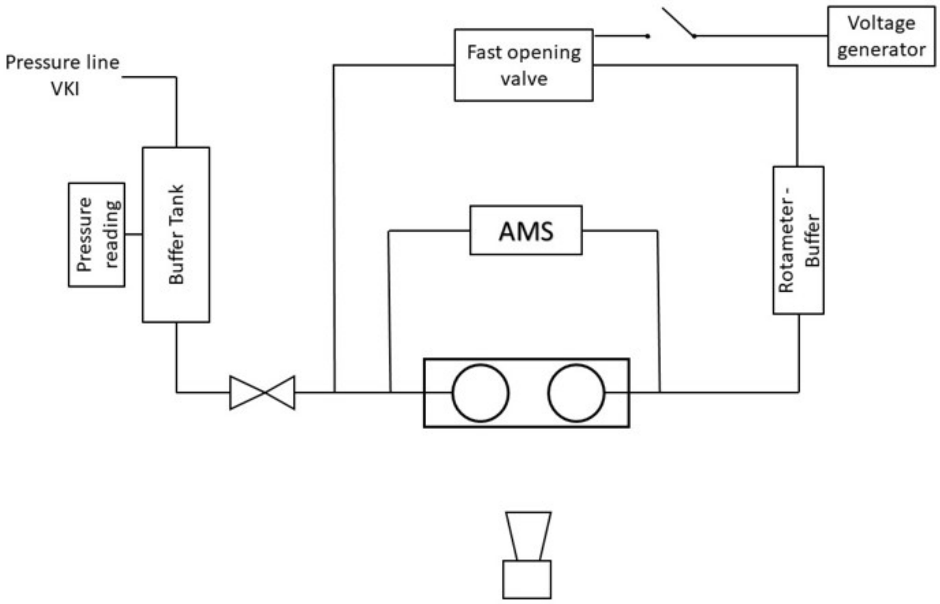

Figure 2.3: Experimental setup

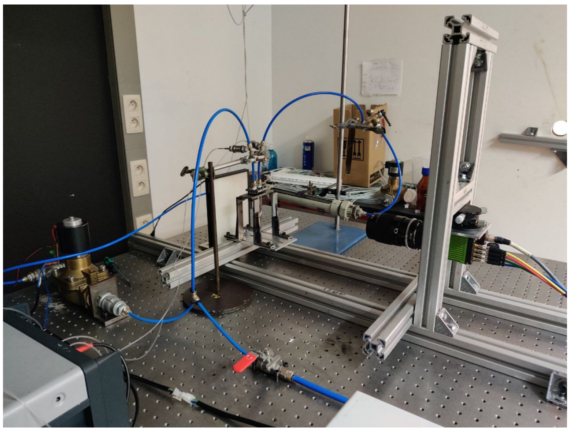

Figure 2.4: Experimental setup side sx

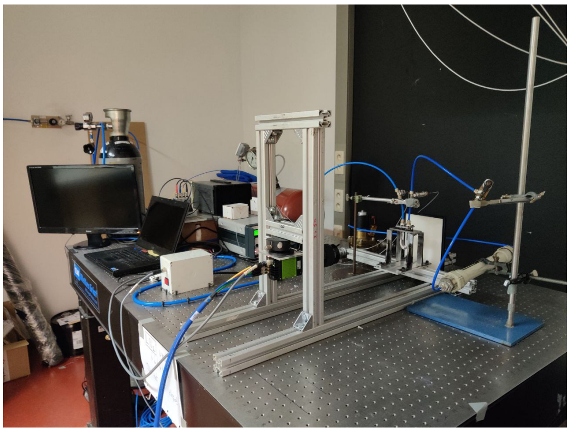

Figure 2.5: Experimental setup side dx

The schematic diagram of the experimental setup is summarised in Fig. 2.6. It shows the two sides of the tube, side A and side B, that are connected by flexible pipes, and a fast-opening valve regulates the flow between them. At the inlet of each side, there are two AMS 5812 piezoresistive pressure sensors manufactured by Analog Microelectronics. Side A is connected to a pressure line, while side B is connected to a discharge pressure line. The initial phase of the experiment consists in cleaning the tube with a small amount of isopropanol solution (approximately 2 ml) to remove any impurities and contaminants that may affect the accuracy and reliability of the measurements made inside the tube. Isopropanol evaporates quickly without leaving any residue, making it ideal for cleaning delicate surfaces such as quartz.

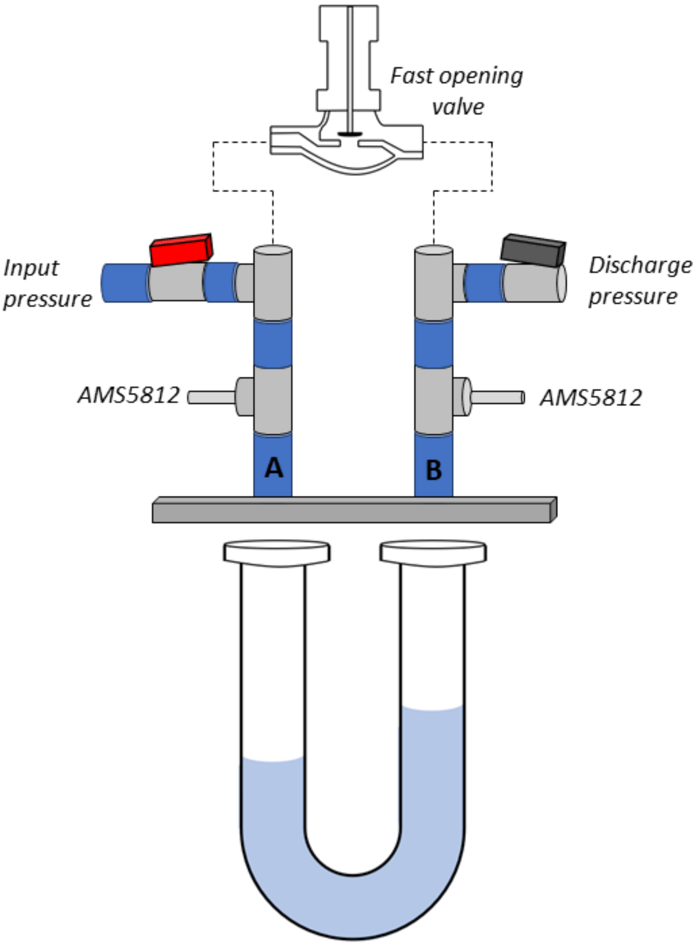

Figure 2.6: Schematic diagram of the experimental setup

After rinsing the tube for a few seconds, we proceed with the drying process, which takes at least two hours to ensure the presence of only one species inside the tube.

Initially, the U-tube is filled with the liquid to be tested while the fast-opening valve is open, thus achieving equilibrium between the two columns of liquid. The initial conditions are established by closing the fast-opening valve and applying a certain pressure that will create a difference in the level inside the U-tube. The preparatory phase concludes by closing all connections with the external environment and allowing sufficient time for the gas volume inside the tube to reach saturation. It is assumed that there is no evaporation of the gas-liquid interface during the experiments to maintain the saturation conditions. These measures ensure that the experiment is conducted under consistent and reliable conditions.

The experiment begins by opening the fast-opening valve, which brings the two sides A and B of the U-tube into contact. As a result of this input, the two interfaces start to oscillate around the equilibrium condition.

2.1.1 Camera settings

The moving interface of one of the two columns, side A, is recorded with a high-speed SP-1200-CXP4 camera acquiring at 300 fps.

The interface is made visible by a LED light placed behind the tube. We reduced the region of interest, ROI, to 640 × 3125 px in order to achieve the highest acquisition frequency of the camera, focusing only on the main subject, the A-side of the tube.

Figure 2.7: SP-1200-CXP4 camera

Since the interface moves at tens of cm/s, it is possible to estimate the exposure time, i.e. the time during which the camera's sensor is exposed to light.

$$Exposure\ time = \frac{Max\ allowed\ image\ blur\ in\ pixels}{Conveyor\ belt\ speed} \cdot \frac{Horizontal\ part\ size}{Sensor\ size\ in\ pixels} \tag{2.1}$$

Thus, the exposure time can be estimated as:

$$Exposure\ time = \frac{0.5\ pix}{10\ cm/s} \cdot \frac{1.2\ cm}{800\ pix} = 75\ \mu s$$

The camera settings used are:

- ROI: 640 × 3125 px
- Pulse frequency: 300 Hz
- Exposure time = 100 μs
- F# number: 5.6

The pixel size is calculated as 14 mm/640 px for the first tube and 12 mm/640 px for the second one.

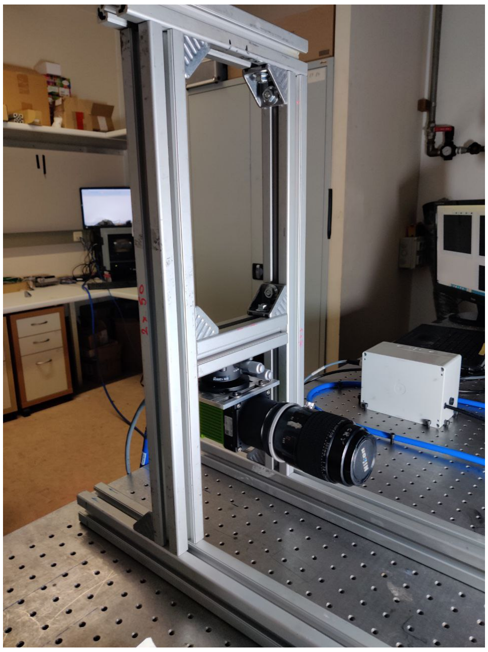

Figure 2.8: CXP4 + micro-Nikkor 105mm

The camera mounts a Nikon micro-Nikkor 105mm lens and is mounted on a bosch profile structure that allows movement in all directions, in order to allow a rapid change of setup between the first and second tube.

2.1.2 Pressure measurements

In the field of experimental fluid dynamics, one element of fundamental importance is the evaluation of pressure and velocity fields.

Often, and this also applies to the experiment described in this work, pressure measurements are made under non-stationary conditions. A common example is when the pressure varies over time, in which case the frequency response and the effects of various parameters must be taken into account. In each situation, the pressure signal recorded over time referred to as P, will usually differ from the actual pressure over time, called P_{true}. This difference can manifest itself in various forms, such as an oscillating or non-oscillating response, and small or large damping, as shown in Fig. 2.9. In all these cases, it is necessary to know the "response time", i.e. the time interval within which the pressure value reaches the steady-state value.

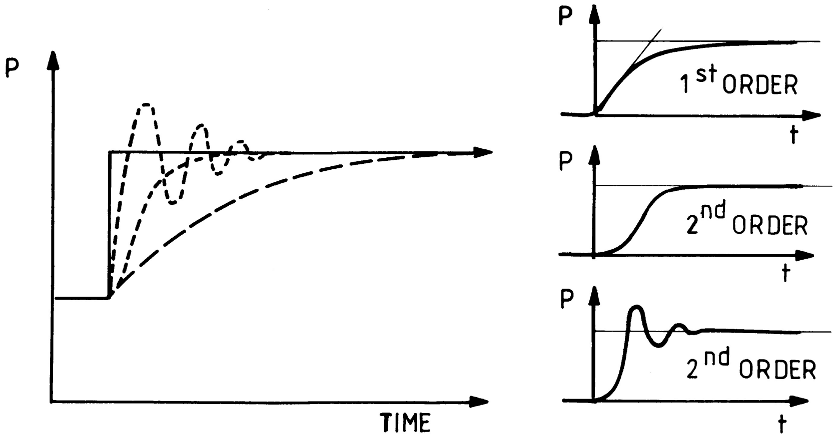

Figure 2.9: Time response to a pressure step [21]

According to [21] there are three examples in which a system frequency response is converted into a step response.

In the case of the experiment described in this paper, the two AMS 5812 pressure sensors are positioned at the outlet of the U-shaped tube. Following the opening of the Fast-Opening Valve (FOV), the pressure will have a frequency response to a step response. To avoid excessive oscillations of the pressure signal, a cavity volume can be used. In this case, a rotameter is inserted into the B side of the U-shaped tube, which acts as a volume to dampen oscillations.

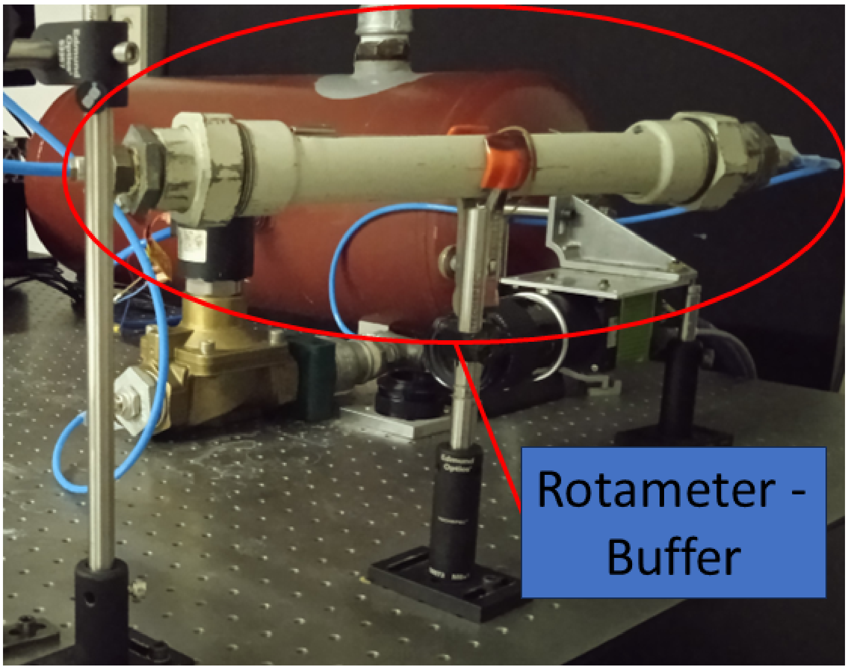

Figure 2.10: Rotameter

2.1.3 Calibration

The calibration of pressure sensors is the process of determining the relationship between the known applied input pressure of a sensor and its output signal, in this case, a voltage. The relationship found is the calibration curve, which is supposed to be linear.
Calibration is essential to ensure accuracy and reliability in the experimental phase.

Figure 2.11: AMS

The pressure sensors used are the AMS5812-0003-D-B Amplified Low Pressure Sensor operating between -20.68 to +20.68 mbar. This range was divided into 30 intervals corresponding to 31 pressure values. The pressure values were given using a DPI 610 pressure calibrator, a multifunctional calibration instrument manufactured by GE Druck. Using an NI 9215, a data acquisition card (DAQ) manufactured by National Instruments (NI), it was possible to acquire voltage data.

Figure 2.12: Calibration setup

Data acquisition is delegated to a Labview program consisting of a loop within which there is a DAQ assistant and a Write to Text File Function. After setting a pressure value on the calibrator and waiting for it to stabilize, data acquisition begins, which is done for about 5 seconds.

After detecting all values in the desired range, the data is processed using a Python code that returns the mean of the values and the standard deviation.

As the data acquired are volts that have to be transformed into a pressure value, it is better to show the Pressure - Voltage curve.

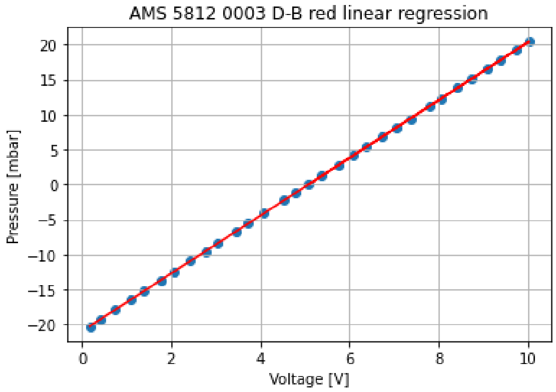

Figure 2.13: Side A sensor $P = f(V)$

Figure 2.14: Side B sensor $P = f(V)$

Uncertainty of the calibration

Uncertainty is evaluated as the root mean square of systematic error and random error sources. AMS pressure sensors are calibrated with a calibrator DPI 310 70 mbar and the uncertainty is given by ±0.05% of reading + ±0.025% of instrument range [22]. The systematic uncertainty is:

$$b_{P0} = \pm 0.05\% \cdot 20.68 \; mbar \pm 0.025\% \cdot 70 \; mbar = \pm 0.02784 \; mbar \tag{2.2}$$

Random uncertainty is evaluated as the standard deviation of the samples in terms of the voltage acquired at a certain sampling frequency for 5 seconds.

$$s_{E_i} = \sqrt{\frac{\sum_{j=1}^{N}(V_j - \bar{V})^2}{N-1}} \tag{2.3}$$

The calibration curve obtained is linear, $P = m \cdot V + q$. Pressure random uncertainty is computed by propagation as:

$$s_1 = \sqrt{\left(\frac{\partial P}{\partial V} s_{E_1}\right)^2 + \left(\frac{\partial P}{\partial V} s_{E_2}\right)^2 + ... \left(\frac{\partial P}{\partial V} s_{E_{N_{cal}}}\right)^2} \tag{2.4}$$

To evaluate the quality of the fitting curve the standard estimate of error is used as:

$$SEE_{P_0} = \sqrt{\frac{\sum_{i=1}^{N_{cal}} (P_{0,i} - P_{0,fit,i})^2}{N_{cal} - K}} \tag{2.5}$$

where $N_{cal} = 31$ and $K = 2$ is the number of coefficients of the calibration curve, which is linear.

$$s_2 = \frac{SEE_{P_0}}{\sqrt{N_{cal}}} \tag{2.6}$$

The total random error source is:

$$s_{P_0} = \sqrt{s_1^2 + s_2^2} \tag{2.7}$$

The uncertainty for the pressure and its expansion value at 95% confidence level are:

$$U_{P_0} = \sqrt{s_{P_0}^2 + b_{P0}^2} \tag{2.8}$$

$$U_{P_{0,95\%}} = 2 \cdot U_{P_0} \tag{2.9}$$

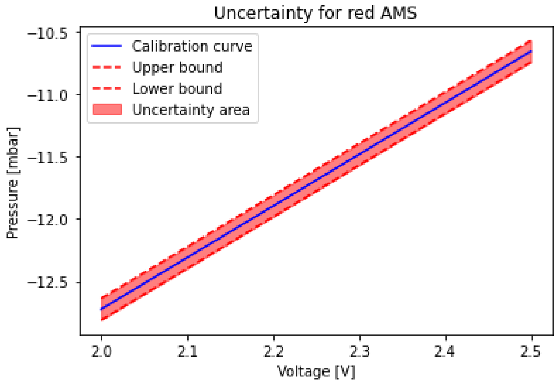

Figure 2.15: Side A sensor uncertainty

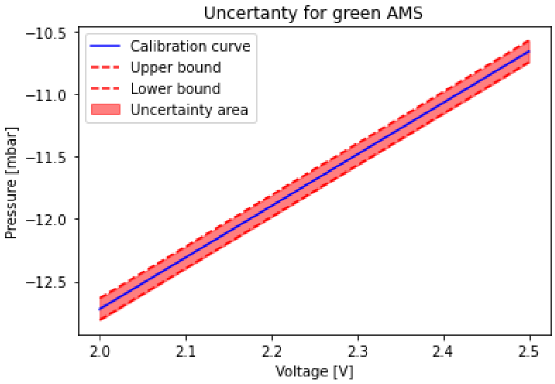

Figure 2.16: Side B sensor uncertainty

2.1.4 Scaling analysis

The dynamic of the liquid interface inside a U-tube is described by means of a one-dimensional ordinary differential equation (ODE), which is obtained by applying the integral balance of forces acting on the liquid column.

As shown by Fiorini et al. [23], the forces at play are:

- viscous resistance $F_\mu = 4f\frac{L}{D}\frac{1}{2}\rho\nu^2 A = \frac{8\mu}{R^2}L\nu A$
- gravity $F_g = 2\rho g h A$
- interface pressure drop $F_p = \Delta P A$

considering the laminar regime assumption, thus $f = 16/Re$.

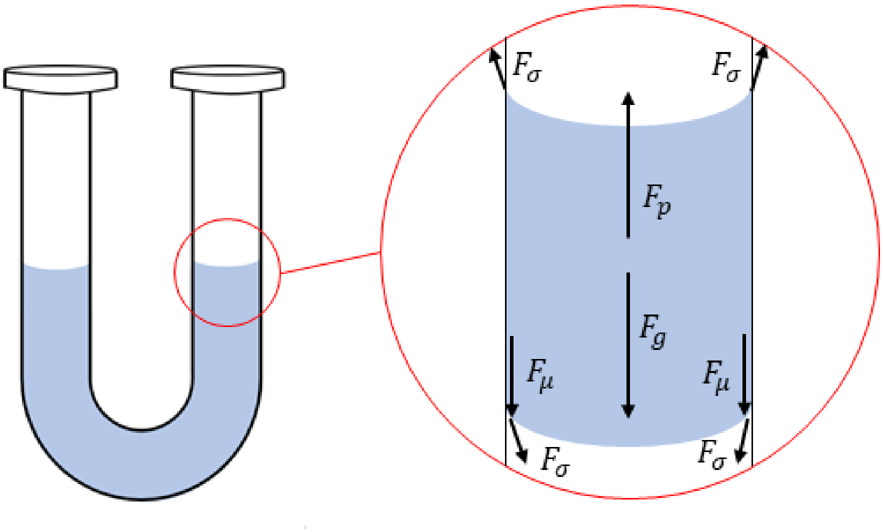

Figure 2.17: Balance of forces

We define $\bar{h}$ as the spatial average over the meniscus. The model reads as:

$$\ddot{\bar{h}} = -C_f 8\frac{\mu}{\rho R^2}\dot{\bar{h}} - \frac{2g}{L}\bar{h} - \frac{2\sigma}{\rho R^2 L}(K_A - K_B) \tag{2.10}$$

K_A and K_B represent the integral of the pressure drop at the liquid interface on each side of the U-tube. The term C_f is a correction term that takes into account the transient behavior of the fluid. The viscous resistance formulation assumes that $C_f = 1$ when the radial velocity profile corresponds to the ideal Poiseuille profile along the tube axis.

Equation 2.10 can be written in dimensionless form. Calling a, b, and c the constant terms of the Equation 2.10, we can write:

$$\frac{[h]}{[t]^2}\ddot{\hat{h}} = -a\frac{[h]}{[t]}\dot{\hat{h}} - b\hat{h} - c\left(\hat{K}_A - \hat{K}_B\right) \tag{2.11}$$

$$\ddot{\hat{h}} = -a[t]\dot{\hat{h}} - b[t]^2\hat{h} - c[t]^2\left(\hat{K}_A - \hat{K}_B\right) \tag{2.12}$$

We can use the oscillating period as a reference time, $t_{ref} = \sqrt{L/2g}$:

$$\ddot{\hat{h}} = -\sqrt{32}\phi^2\frac{1}{Re}\sqrt{\frac{h_0}{L}}\dot{\hat{h}} - \hat{h} - \frac{1}{We}\frac{h_0}{R}(\hat{K}_A - \hat{K}_B) \tag{2.13}$$

where $\phi = L/R$ is a geometry factor, h_0 is the initial difference of height, and $u = g \cdot h_0$ is the reference velocity.

In the dimensionless equation, one can recognise the two dimensionless groups Π_1 and $\Pi3$.

$$\Pi_1 = \sqrt{32}\phi^2\frac{1}{Re}\sqrt{\frac{h_0}{L}}$$

$$\Pi_3 = \frac{1}{We}\frac{h_0}{R}$$

A comparison of fluids properties of demineralized water, HFE7000 and HFE7200, and liquid hydrogen and liquid oxygen is shown in Tab. 2.2. The properties of water and the HFEs are under standard conditions, while in the case of Liquid Nitrogen at $T = 77K$ and for Liquid Oxygen at $T = 90K$.

		Dem. Water	HFE7200	HFE7000	LN_2	LOX
Density (ρ)	kg/m^3	997	1423	1400	807	1141
Dynamic viscosity (μ)	$mPa\ s$	0.97	0.64	0.49	0.147	0.195
Surface tension (σ)	mN/m	72.01	13.62	12.4	8.94	13.2

Table 2.2: Fluids properties

A comparison of the nondiminesional groups between the proposed liquids is then presented, under two conditions, low gravity condition $0.1 \cdot g$ and gravity condition g.

Low-g conditions

	Dem. Water	HFE7200	HFE7000	LN_2	LOX
Π_1	0.6890	0.3184	0.2275	0.1289	0.1210
Π_3	337.032	44.647	41.316	51.676	53.965

Table 2.3: Comparison of nondimensional groups for low-g conditions

Ground conditions

	Dem. Water	HFE7200	HFE7000	LN_2	LOX
Π_1	0.0696	0.0321	0.0230	0.0130	0.0122
Π_3	3.4356	0.4551	0.4212	0.5268	0.5501

Table 2.4: Comparison of nondimensional groups for ground conditions

An analysis of the dimensionless groups reveals a considerable gap between the characteristics of demineralised water and space propellants. However, what is of greatest interest is HFE7000, whose properties approach those of liquid oxygen and liquid hydrogen.

For both case studies, under low gravity and ground conditions, Π_1 and Π_3 vary similarly and have the same order of magnitude when it comes to HFE7000 and space propellants. An interesting aspect to note is that under microgravity conditions, the dimensionless group Π_3 prevails over Π_1. This suggests that capillarity forces play a predominant role over other influences.

2.1.5 Experimental campaign and test matrices

The experimental campaign begins with the first tube with internal diameter $D = 8\ mm$ and axial length $L = 164\ mm$.

The U-tube was tested with three different filling levels and with theoretical Δh calculated as:

$$\Delta h = \frac{\Delta p}{\rho g}$$

Once the value of Δp with which to fill the tank has been established, the experiment begins.

The pressurization valve is opened to obtain a Δh, as shown in Fig. 2.20, and once the liquid is stabilized, the fast opening valve is opened, which connects the two sides of the pipe, causing the liquid inside the pipe to oscillate until the equilibrium condition is reached. The test is concluded by opening the discharge pressure valve discharging the pipe and returning it to its initial condition, Fig 2.19.

Every single experiment was repeated three times for repeatability analysis. Fig. 2.18 shows an example of this analysis where the relative displacement curves overlap.

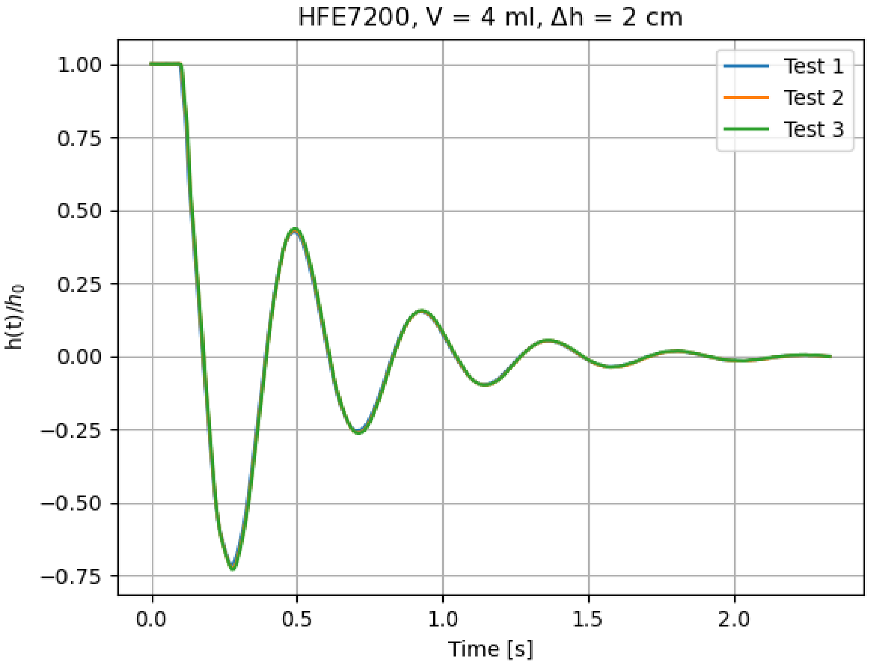

Figure 2.18: Repeatability analysis

Figure 2.19: Equilibrium condition

Figure 2.20: Initial condition

Tests conducted with the first tube are shown in Tab. 2.5.

	HFE7200	HFE7000	Dem. Water	Isopropanol	Ethanol	Diprop. Glycol
$V = 3.5\ ml,\ \Delta h = 1\ cm$	✓	✓				
$V = 4\ ml,\ \Delta h = 1\ cm$	✓	✓				
$V = 4\ ml,\ \Delta h = 2\ cm$	✓	✓	✓	✓	✓	✓
$V = 4\ ml,\ \Delta h = 3\ cm$	✓	✓				
$V = 4.5\ ml,\ \Delta h = 1\ cm$	✓	✓				

Table 2.5: Test matrix tube with $D = 8\ mm$ and $L = 164\ mm$

Tab 2.6 shows the tests carried out with the tube with an internal diameter of $D = 7\ mm$ and axial length of $L = 198\ mm$.

	HFE7200	HFE7000	Dem. Water
$V = 2.7\ ml,\ \Delta h = 1\ cm$	✓	✓	
$V = 3.1\ ml,\ \Delta h = 1\ cm$	✓	✓	
$V = 3.1\ ml,\ \Delta h = 2\ cm$	✓	✓	
$V = 3.1\ ml,\ \Delta h = 3\ cm$	✓	✓	
$V = 3.5\ ml,\ \Delta h = 1\ cm$	✓	✓	✓
$V = 3.5\ ml,\ \Delta h = 2\ cm$	✓	✓	
$V = 3.5\ ml,\ \Delta h = 3\ cm$	✓	✓	

Table 2.6: Test matrix tube with $D = 7\ mm$ and $L = 198\ mm$

The filling volume was determined so that the axial length of the liquid was the same during the tests on the two tubes.

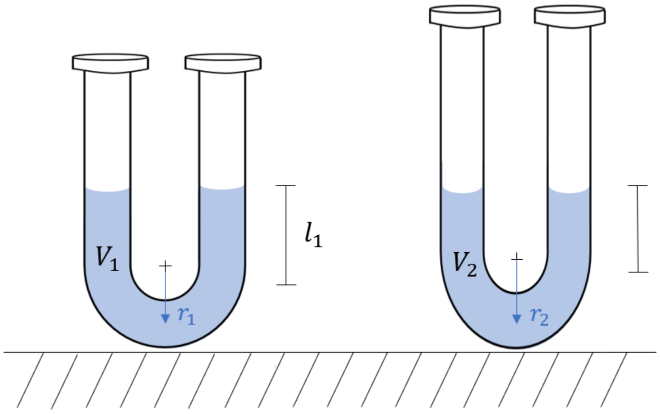

Figure 2.21: The two U-shaped tubes used for experimentation

According to the nomenclature in Fig. 2.21, the two axial lengths must be equal.

$$L_1 = L_2$$

$$2 \cdot l_1 + \pi \cdot r_1 = 2 \cdot l_2 + \pi \cdot r_2$$

Since the second tube has a smaller internal diameter than the first, the second volume will be smaller than the first.

2.2 Image analysis

The experimental images, an example is shown in Fig. 2.22, were analyzed with an image processing algorithm written in *Python* that includes several steps.

The first step consists of increasing the overall brightness of the image to improve the visualization of the interface and establish standard conditions for all images.

Figure 2.22: Static interface, experimental image

Next, the pixels are processed through a remapping process, which aims to delete some of the less relevant details in the image background.

Subsequently, the image is subjected to a threshold filter to convert the image into a binary form, in which pixels are separated into two categories: those above the threshold and those below. This step is called "image binarization".

Next, the "findcontours" function provided by the OpenCV library (cv2) is exploited. This function can find and trace the contours in the image, creating a set of edges. These detected contours are then superimposed on an empty image, thus creating a visualization of the detected edges. The 'step 2' is reached and can be observed in Fig. 2.23b.

A second function performs the task of identifying the boundary between the white and black areas in an image. Initially, the image is cropped laterally until it reaches the inner edge of the U-tube, using reference values provided by the user. Subsequently, the edge

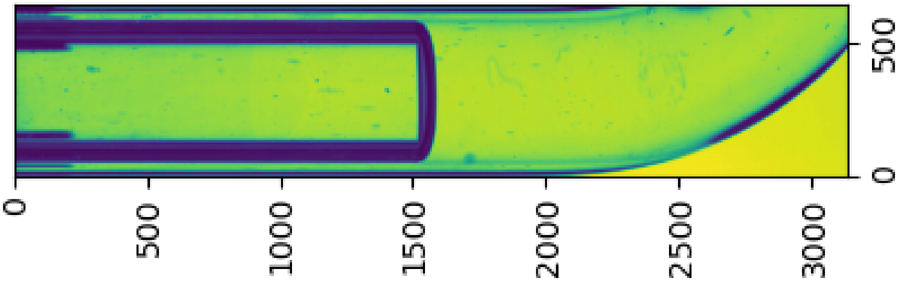

(a) Step 1

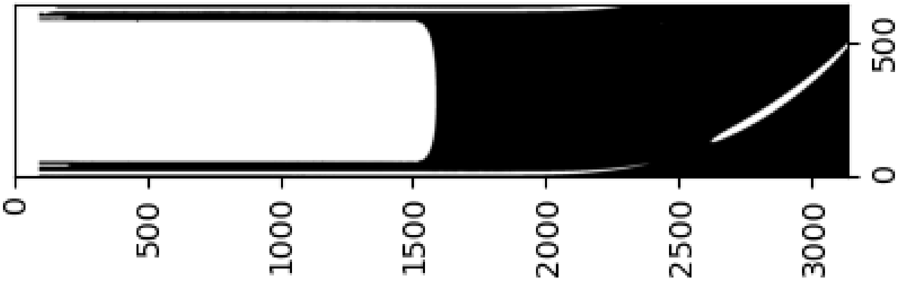

(b) Step 2

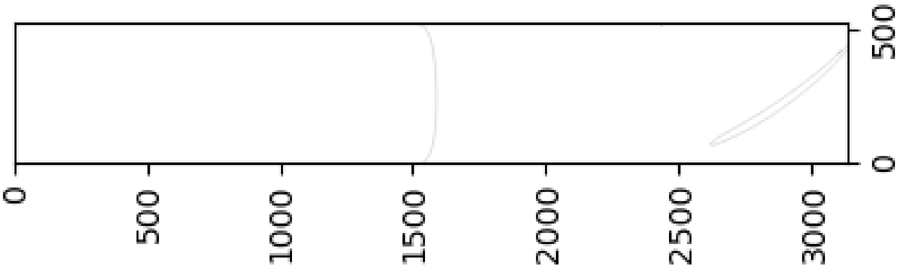

(c) Step 3

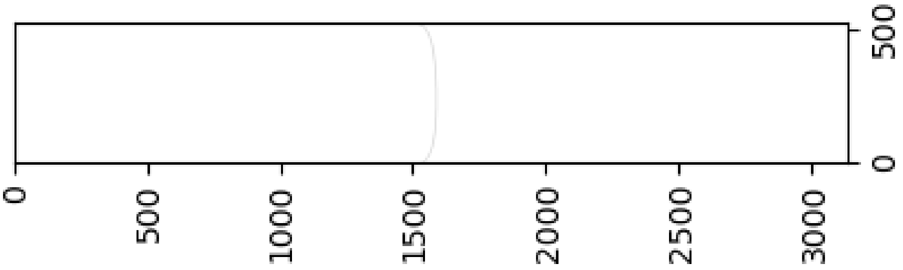

(d) Step 4

Figure 2.23: Edge detection process

detection process is carried out in the following way: each pixel with a value below the threshold of 128, therefore considered as white, is examined together with the surrounding pixels. If black pixels are detected in the nearby, the point at which the boundary between the two shades is identified. At the end of this process, Fig.2.23c is obtained. Afterward, the processed image undergoes a cleaning process through a dedicated function, the purpose of which is to remove any noise. In particular, the pixels corresponding to the curved portion of the U-tube are rendered black. This choice derives from the fact that the main purpose of this study does not contemplate the detailed analysis of the dynamics of this section.

In a further step, the image is vertically scanned in bands of 50 pixels each. The aim is to identify the band with the highest concentration of white pixels. This band represents the area of the interface of interest, while the rest is automatically rendered black. The final image is shown in Fig. 2.23d.

2.2.1 Optical correction

To determine the true contact angle between the liquid and the tube wall, an optical correction is necessary. Objects inside cylindrical tubes appear distorted when observed from outside the tube due to the refraction of light as it passes through different mediums. Using the approach of Darzi and Park [24], a correction can be calculated given the tube features and the distance of the camera. Using the external diameter of the tube as a reference, we measure the image scaling and obtain the physical size of the pixels in each image. This corresponds to 20 μm along the channel axis for the experiment with the first tube and 16.9 μm for the experiment with the second tube.

Under the assumption that the vertical portion of the U-shaped tube has an axial symmetric profile and there is no curvature in the axial direction, the images are optically distorted in the radial direction only.

Figure 2.24 shows the trigonometric scheme used to find the optical deviation of point A to point B. To obtain the coordinates of point B, the quantities $\overline{\text{NB}}$ and Ω must be determined. Initially, the triangle OBN is taken, and the angle g is determined, knowing

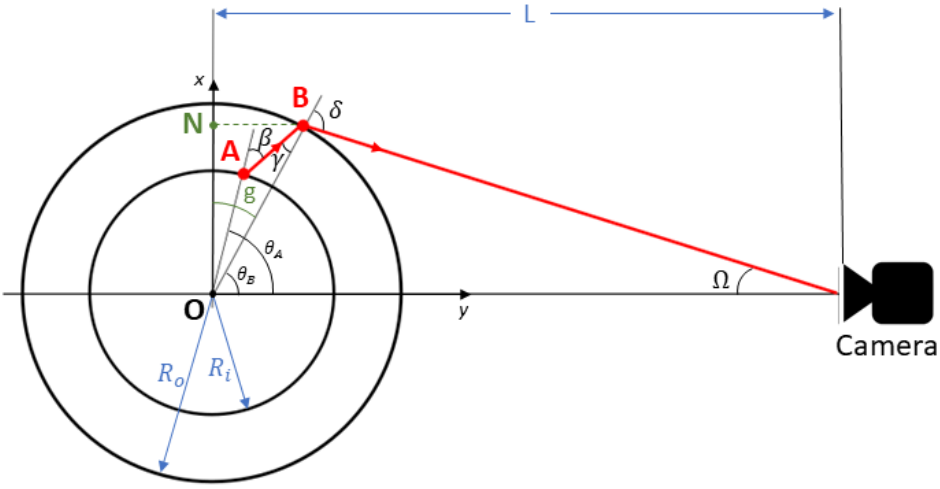

Figure 2.24: Optical correction for a single-camera setup [24]

the outer radius of the tube.

$$g = \arccos\left(\frac{x}{R_o}\right)$$

Thus, it is possible to find $\overline{\mathrm{NB}}$ and the y coordinate of the point B, h_1.

$$\overline{\mathrm{NB}} = R_o \cdot \sin g$$

$$h_1 = L - \overline{\mathrm{NB}}$$

Calling "x" all the x-coordinates of the points B, it is possible to calculate the angle Ω.

$$\Omega = \arctan\left(\frac{x}{h_1}\right)$$

The light ray, coming from behind the tube, passes through point A and is deflected due to the refractive index of the quartz n_w to point B. The ray arriving at the chamber is deflected by an angle δ to the line passing through OB.

$$\beta = \arcsin\left(\frac{n_o}{n_w}\frac{L}{R_i}\sin\Omega\right)$$
$$\gamma = \arcsin\left(\frac{n_o}{n_w}\frac{L}{R_o}\sin\Omega\right)$$
$$\delta = \arcsin\left(\frac{L}{R_o}\sin\Omega\right)$$

Define a possible misalignment θ_0, the angles θ_A and θ_B are determined by the angle relations as follows:

$$\theta_A = \delta + \beta - \gamma - \Omega + \theta_0$$
$$\theta_B = \delta - \Omega + \theta_0$$

Thus, the correction is given by the minor cathetus of triangle ABM.

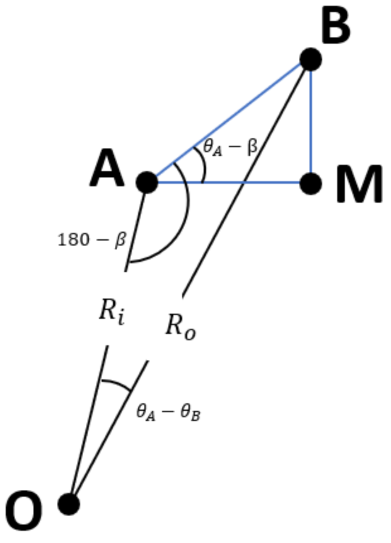

Figure 2.25: Detail ABM triangle

$$correction = R_o \cdot \frac{\sin(\theta_A - \theta_B)}{\sin(180 - \beta)} \cdot \sin(\theta_A - \beta)$$

The actual coordinate hit can be calculated as:

$$x_{corr} = x - correction$$

Figure 2.26 shows three optical correction made in the reference case with HFE7200, $V = 4\ ml$ and $\Delta h = 2\ cm$.

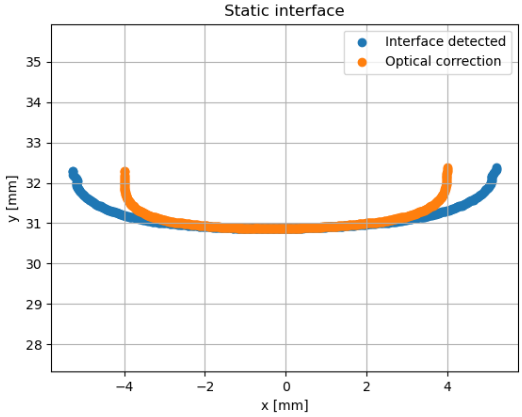

(a) Static configuration

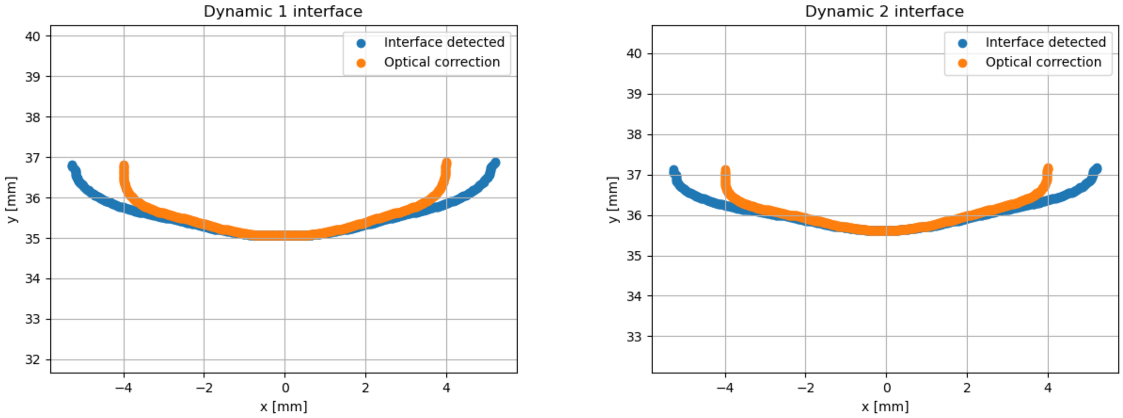

(b) Dynamic configuration 1 (c) Dynamic configuration 2

Figure 2.26: Optical correction of three frames of case $V = 4\ ml$ and $\Delta h = 2\ cm$

2.3 Experiment uncertainty

HFEs are characterized by high volatility, which makes laboratory tests difficult to replicate. A study on the uncertainty of experimental tests is therefore conducted.

We propose two approaches; the first one involves calculating an uncertainty band for the displacement data obtained during the three tests of a single experiment. This would make it possible to determine how reliable the results are and how much variability there may be in the data due to possible experimental errors or fluctuations in the fluids.

The second approach focuses on the control of interfaces, both under static and dynamic conditions.

A displacement analysis for a particular case with HFE7200 is shown in Fig. 2.27.

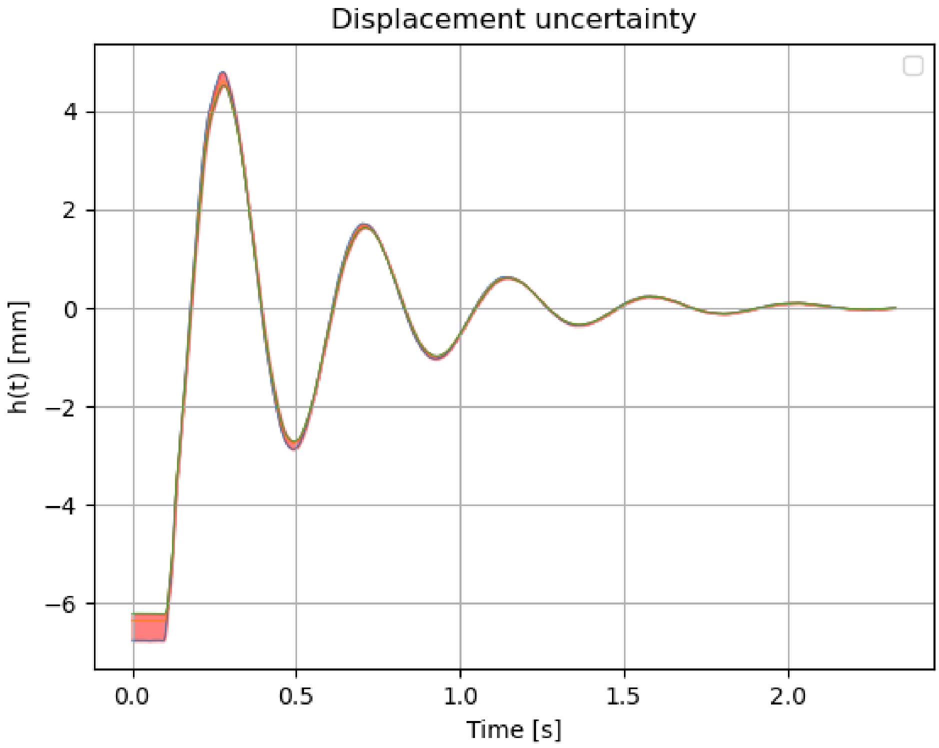

Figure 2.27: Displacement uncertainty for the experiment with 4 ml of HFE7200 and $\Delta h = 2\ cm$

The average thickness of the band between the curves for this case is $0.0794\ mm$.

Even though the tests were carried out in succession, a certain amount of liquid was lost between one test and another. This discrepancy can be seen in the first part of the graph, where the initial liquid heights for each test are represented. Despite this, the tests show very good repeatability. Knowing the tube radius $R = 4\ mm$, it is possible to estimate the total amount of volume lost by evaporation between one test and another, $V_{lost} = \pi R^2(h_3 - h_1) = 0.028\ \mu l$.

The second test performed shows the interfaces of a static case at $t = 0\ s$ and a dynamic case at $t = 0.14\ s$.

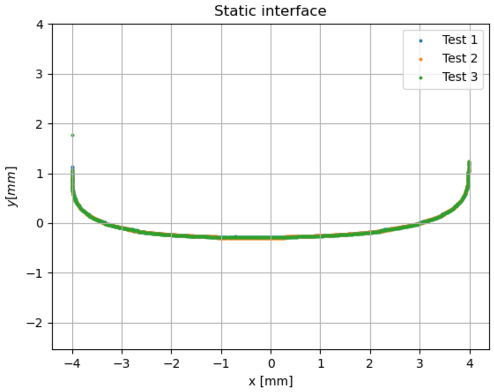

Figure 2.28: Comparison between static interfaces of three tests with HFE7200, at $t = 0\ s$

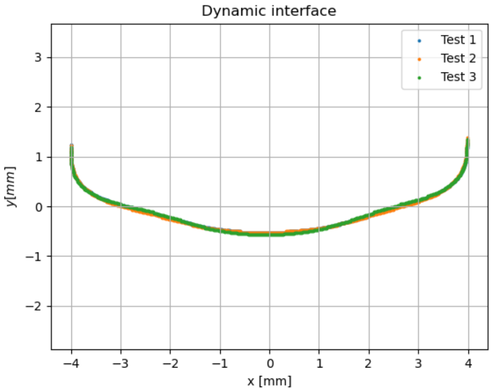

Figure 2.29: Comparison between dynamic interfaces of three tests with HFE7200, at $t = 0.14\ s$

Interfaces occurring at the same time instant can be superimposed.

This analysis, together with the previous one, shows that the tests are repeatable and that it is possible to replicate the experiments by obtaining test cases with the same dynamics.

2.4 Modeling

Analyzing the experimental points that trace the interface during the experiment, it is observed that the points close to the wall are difficult to detect with accuracy. Finding contact angle values using only the experimental data therefore leads to an overestimation of the contact angle, as confirmed by Fiorini et al [19].

In this work, we used two different approaches: the Meniscus Profile Method, MPM approach in comparison with Support Vector Regression, SVR.

The MPM approach consists of fitting experimental data with models, using the contact angle as a parameter. Contact angle values are obtained via a regression problem.

SVR is instead a machine learning technique used for regression, which is based on the concept of Support Vector Machines (SVM). SVR seeks to find a function that approximates the training data while minimizing error.

2.4.1 Inertial-less model

Under static conditions, the shape of the interface is controlled by the balance of gravitational and capillary forces. This shape is axisymmetric.

Using the reference system r, y, z, located at the center of the channel with origin at the interface, as shown in Fig. 2.30, the balance can be written:

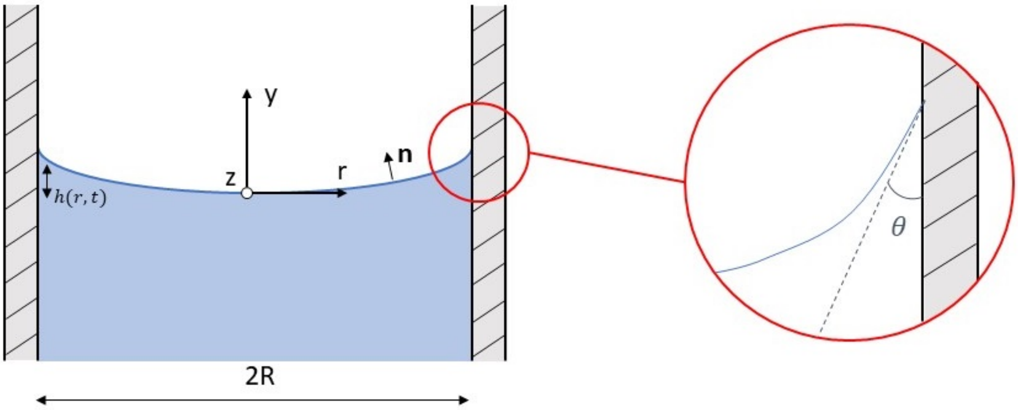

Figure 2.30: Interface model

$$\sigma \nabla \cdot n + \rho g h = 0 \tag{2.14}$$

where n is the unit normal vector and $\nabla \cdot n$ is the interface curvature. With h_r and h_{rr} as the first and second derivatives of h in the coordinate r, it is possible to define the normal and consequently the curvature as:

$$n = \frac{z - h_r r}{1 + h_r^2}, \quad \nabla \cdot n = \frac{-r h_r - r^2 h_{rr}}{r^2 (1 + h_r^2)^{3/2}}$$

The equation 2.14 can be rewritten by introducing the capillary length $l_c = \sqrt{\sigma/\rho g}$ which relates the gravity forces to surface tension.
The equation is solved with Neumann conditions at the wall and Dirichlet conditions at the center of the channel, assuming that the interface is flat in a region of the origin.

$$\begin{cases} \nabla \cdot n + l_c^{-2} = 0, \\ h_r(R, t) = ctg(\theta(t)), \\ h_r(0, t) = 0 \end{cases} \tag{2.15}$$

The model described uses $\theta(t)$ as the dynamic contact angle. The model 2.15, called quasi-static, offers a good approximation for static interfaces or interfaces moving at low speed.
The model 2.15 does not take into account viscous forces, which must be considered when the column of liquid begins to oscillate. With the Voinov approximation the viscous pressure can be approximated as:

$$\Delta p_\nu = 3 \frac{\mu U_{cl}}{R - r} F(\beta) \tag{2.16}$$

$F(\beta)$ is a correction factor for small slopes of the interface that can be calculated as: $F(\beta) = \dfrac{\sin \beta(r)}{\beta(r)^2}$ with $\beta = cotg(h_r)$.
Definig the capillary number as $Ca = \mu U_{cl}/\sigma$ the model can then be corrected as follows:

$$\begin{cases} \nabla \cdot n + l_c^{-2} - 3 \dfrac{Ca}{R - r} F(\beta) = 0, \\ h_r(R, t) = ctg(\theta(t)), \\ h_r(0, t) = 0 \end{cases} \tag{2.17}$$

The model 2.17 is valid for moderate contact line accelerations.

The problem of the shape of a meniscus, showed in the system 2.15, is solved numerically with a boundary value problem, BVP. The shape of the meniscus is governed by ordinary differential equation:

$$h''(x) = \frac{h(x)}{l_c^2}\left(1 + (h'(x))^2\right)^{3/2} - \frac{h'(x)}{x} \tag{2.18}$$

In order to solve the problem, it is necessary to specify the boundary conditions, which in this case are as follows: $h_r(R,t) = ctg(\theta(t))$ on the wall of the pipe and $h_r(0,t) = 0$ in the central part of the tube.

To solve the boundary value problem, SciPy's *solve_ bvp* function is used, which attempts to find a numerical solution of the ODE subject to the specified boundary conditions.

We denote with $h(r, w(t))$ the interface profiles that solve problem 2.15 at time t, parametrized by the parameter set $w(t) := \theta(t), c(t)$, where θ is the contact angle and c c is the height of the interface midpoint.

The regression aims to find a set of parameters $w(t)$ that will allow the best possible approximation of the interface model $h(r, w(t))$ using the N experimental data (r_i, h_i).

To assess the accuracy of the regression, one can use the Euclidean distance d_i between the experimental points and the interface plus a regularisation term $f_{reg}(\lambda_{reg}, w(t))$ which depends on the regularisation coefficient λ_{reg} and the optimization parameters $w(t)$.

During the trial and error process, we identified that the part of the interface close to the wall is particularly difficult to optimize. To overcome this issue, we introduced weights, denoted χ_i, which allow us to apply a more severe penalty in this specific area.

The best set is the one that minimizes the objective function.

$$\text{argmin}_w \; J(w) = \sum_i^N (d_i(r_i, h_i, h(ri, w(t)))\chi_i) + f_{reg}(\lambda_{reg}, w(t)) \tag{2.19}$$

Optimization was performed using the Nelder-Mead algorithm as the optimization method by SciPy's *minimize* Python library.

2.4.2 Support vector regression

Support Vector Regression (SVR) is a technique that deals with regression problems. The fundamental objective of SVR is to find a band around the training points, which are the data used to teach a learning model how to behave. This band represents a range within which the model can fit. The SVR aims to maximize the width of this band while allowing a certain degree of error controlled by a parameter called ε.

The implementation of the SVR involves the use of kernels, including the radial-based kernel (RBF), which allows the data to be mapped into more complex feature spaces. This helps the model capture non-linear relationships between features and target values, making the SVR suitable for complex regression problems.

The kernel used is the Gaussian RBF, and its mathematical form is:

$$K(x, x') = e^{-\gamma\|\mathbf{x}-\mathbf{x}'\|^2} \tag{2.20}$$

where:

- x is the vector of input data;
- x' is the vector of the centers of each kernel;
- $\|\mathbf{x}-\mathbf{x}'\|^2$ is the squared Euclidean distance between x and x';
- γ is a hyper-parameter that controls how fast similarity decreases with distance.

The formulation of the SVR problem is investigated from a geometric perspective, using the one-dimensional example in Fig. 2.31 [25].

The SVR formulates the function approximation problem as an optimization problem that tries to find a "tube" centered on the data surface, where the tube represents the region within which we want our approximation to fall, the margin zone. The goal is to minimize the prediction error, which is the distance between the model's predicted output and the desired output.

The value of ε affects the width of the tube, with smaller values indicating lower error tolerance and having an impact on the number of support vectors ξ_i, i.e. data points left outside the tube.

The formulation of the SVR optimization problem with Gaussian kernel to be minimized

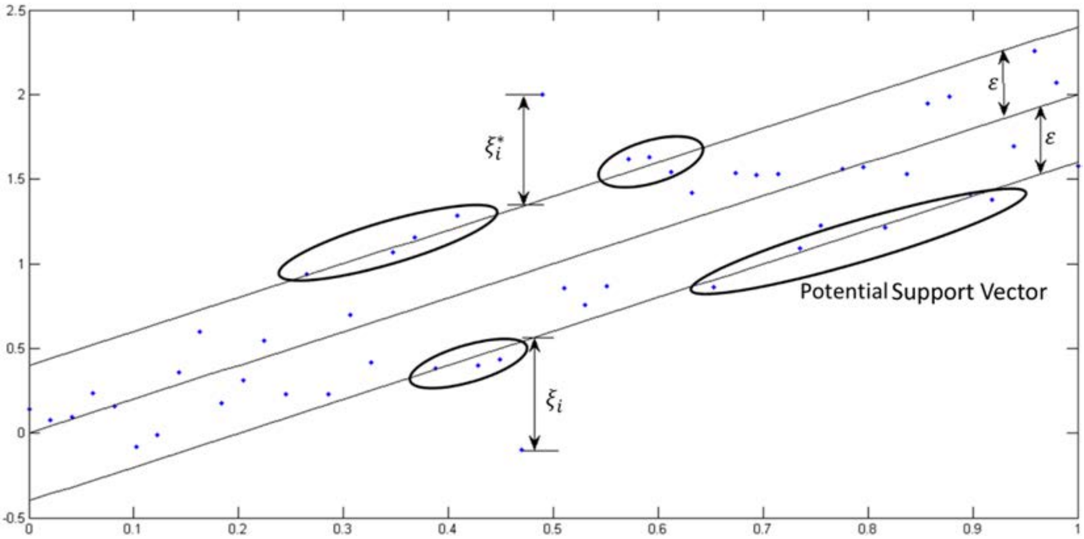

Figure 2.31: One-dimension linear SVR (credits to [25])

is as follows:

$$\text{argmin}_w J(w) = \frac{1}{2} w^T w + C \sum_{i=1}^{N} (\xi_i + \xi_i^*) \tag{2.21}$$

where:

- w is the vector of weights of the regressive function.
- C is a regularisation parameter, i.e. an adjustable parameter that controls the minimization. For example, a larger C gives more weight to error minimization.
- ξ_i and ξ_i^* are slack variables, representing the forecast error for the i-th data point outside the tube.

2.5 CFD description

The problem under investigation is a multiphase problem involving a liquid and a gas inside a U-shaped tube. We investigated numerically this problem using Computational Fluid Dynamics and interFoam solver. The solver belongs to OpenFoam, an open-source platform, and is based on the Volume of Fluid (VoF) method without interface reconstruction. The VoF method is a numerical technique used to trace and solve the interface between two immiscible phases.

To address this problem, we used a three-dimensional, structured mesh, with mesh refinement in the regions where the interface between the gas and liquid is located. This mesh refinement, shown in Fig. 2.35, was adopted to ensure accurate resolution of the separation surface between the two phases.

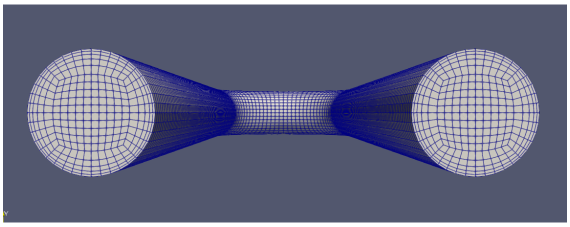

Figure 2.32: Mesh 1

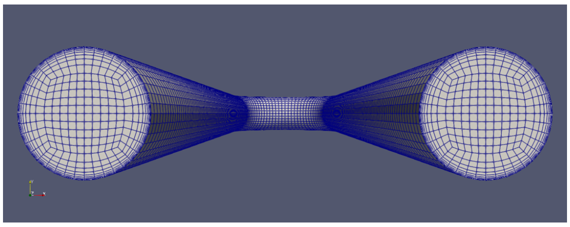

Figure 2.33: Mesh 2

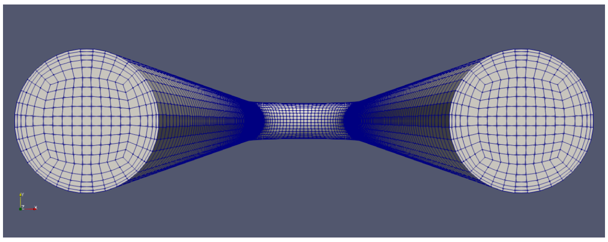

Figure 2.34: Mesh 3

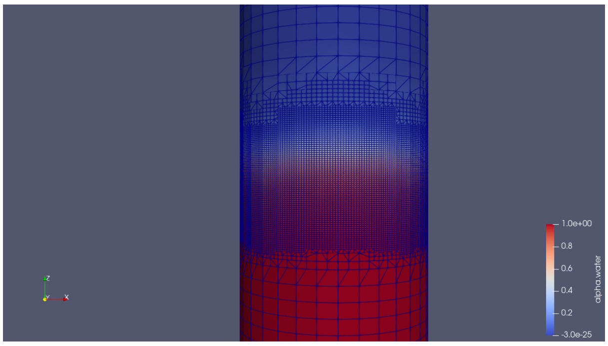

Figure 2.35: Mesh refinement

The concept behind the VoF method is the volume fraction transport equation, α, for a phase:

$$\frac{\partial \alpha}{\partial t} + \nabla \cdot (\alpha \mathbf{U}) = 0 \tag{2.22}$$

where:

- α represents the volume fraction of the phase under consideration, $\alpha = 0$ for gas, $\alpha = 1$ for liquid.
- $\frac{\partial \alpha}{\partial t}$ is the variation in time of α.
- $\nabla \cdot (\alpha \mathbf{U})$ represents the flow of α through the domain.

The *'interFoam'* solver solves this VoF transport equation simultaneously with the Navier-Stokes equations for both phases and thus determines the interface dynamics and fluid behavior. As can be seen in Fig. 2.36, the area of the interface is not sharply defined; instead, there is a gradient of α that varies from 0 to 1. Usually, it is conventional to

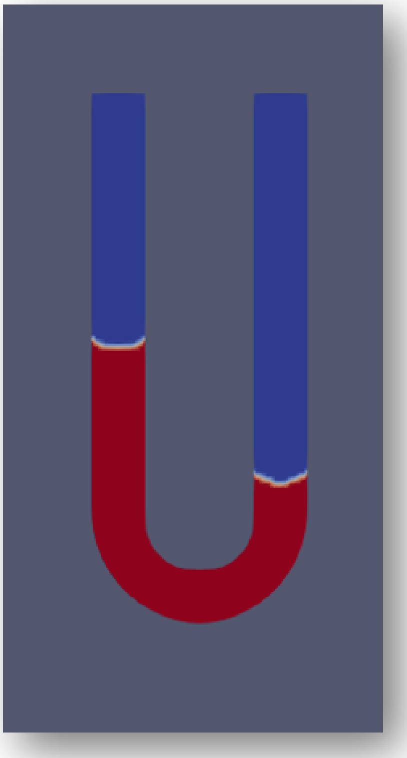

Figure 2.36: CFD initial condition

consider the interface localized at $\alpha = 0.5$.

The boundary conditions for the solution of the problem can be described as follows:

- No slip condition at the wall: This condition implies that the fluid adheres to the wall without flowing along it.
- "Velocity No Gradient" condition at the outlet: This condition implies that the velocity gradient of the fluid along the outlet is zero. This means that the fluid velocity at the outlet is uniform and does not vary along the outlet direction.
- Pressure equilibrium: $p_A = p_B = const$. This means that there is no significant pressure variation between these two specific points in the domain.

The test used as a reference point during CFD simulations implies a liquid volume of $4\ ml$ and a height change $\Delta h = 2\ cm$.

2.6 Evaporation study of HFEs

Since the contact angle is influenced by the chemical composition of the gas phase, it is interesting to know how much HFE evaporates in the tubes during the experimental setup phase. In addition, to carry out numerical CFD simulations with liquid + air mixture and HFE vapours, it is necessary to estimate the properties of the gas in terms of density and kinematic viscosity. Additionally, during the U-tube experiment the liquid evaporates until it saturates the air inside the pipes of the experimental setup. To ensure that the tests are performed always at saturated conditions we assess the evaporation rate of the liquid and estimate the saturation time of the experiment.
This analysis aims to find:

- Evaporation rate of HFEs;
- Density and kinematic viscosity of the mixture of air and HFE vapours;
- Saturation time of the experimental setup volume.

Evaporation rate experiment

Using a precision balance in Fig 2.37, we monitored the evolution of the weight of a certain amount of HFE placed in a dropper. For both liquids, three tests were carried out with different initial amounts of liquid.

Figure 2.37: Precision balance

Figures 2.38 and 2.39 depict how the normalized weight variation for each liquid evolved over time. The slopes of the curves were calculated and compared to obtain the relative evaporation rates of the HFE7200 and HFE7000 liquids. We can observe that HFE7000 is more volatile, as it evaporates more rapidly compared to HFE7200.

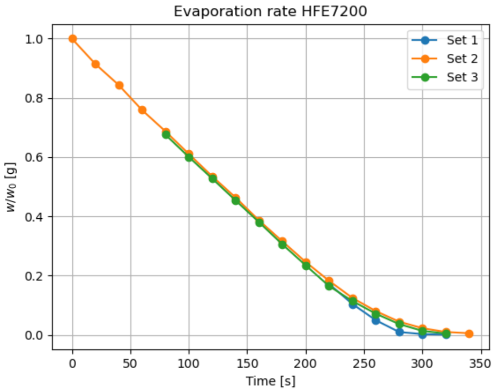

Figure 2.38: Test HFE7200

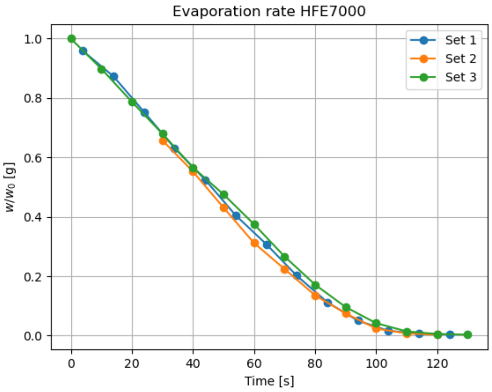

Figure 2.39: Test HFE7000

We compared evaporation results using a linear regression of the experimental data, in Fig. 2.40. However, it is important to exclude points where the data curve shows curvature from the regression, as these points represent the complete evaporation process. In the case of the U-tube, there is partial evaporation of the HFEs.

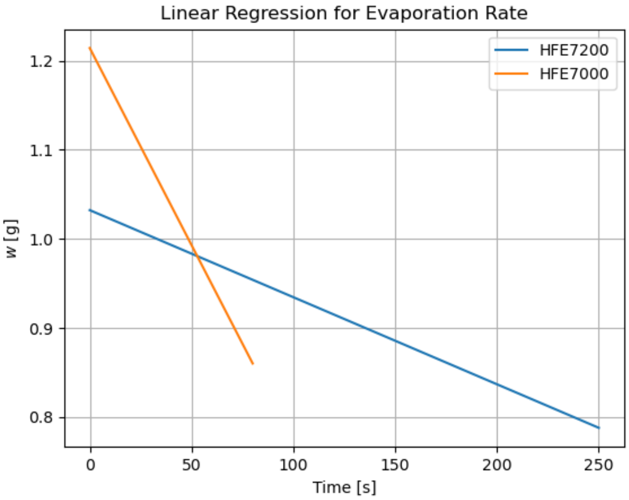

Figure 2.40: Comparison between on the evaporation rate HFE7200 and HFE7000

For simplicity's sake, we have not considered the influence of the drop's exposed surface. This omission is justified by the fact that the tests carried out were aimed at reproducing a situation similar to that in the U-shaped tube, where the drop has a diameter of approximately 1 cm. A detailed discussion considering the influence of the exposed surface of the drop is available in Appendix A.4.2.

The resulting evaporation rate for HFEs is:

- HFE7200: $Evaporation\ rate = 9.775 \cdot 10^{-4}\ g/s$
- HFE7000: $Evaporation\ rate = 4.425 \cdot 10^{-3}\ g/s$

Computation of mixture properties

During the U-tube experiment, the liquid begins to evaporate until it saturates the air inside the pipes of the experimental setup.

The vapor pressure of the HFE7200 is $p_{v_{HFE7200}} = 14.53\ kPa$.

To determine the percentage of HFE in the air, relative pressures can be considered. According to Dalton's law the total pressure of the gas mixture is the sum of the partial pressures of air and HFE vapours.

$$p = p_{air} + p_{v_{HFE7200}}$$

$$p = 101.3\ kPa + 14.53\ kPa = 115.83\ kPa$$

It is then possible to calculate the percentage of HFE7200 present in the gas, as follows:

$$\%HFE7200 = \frac{p_{v_{HFE7200}}}{p} \cdot 100 = 12.54\ \%$$

$$\%Air = 100\% - 12.54\% = 87.46\%$$

The vapour density of the HFE7200 can be estimated from the perfect gas law $pV = nRT$. Knowing that the density can be written as $\rho = m/V$ and that $m = nM$, then:

$$\rho = \frac{nM}{V} = \frac{pM}{RT}$$

The molar mass of HFE7200 ($C_4F_9OC_2H_5$) can be calculated as:

$$M = 12.01 \cdot 6 + 19 \cdot 9 + 16 \cdot 1 + 1.008 \cdot 5 = 264.2\ g/mol$$

thus,

$$\rho_{HFE7200-gas} = 1.55\ kg/m^3$$

Then it is possible to calculate the density of the mixture with a weighted average:

$$\rho_{mixture} = \rho_{HFE7200-gas} \cdot 0.1254 + \rho_{air} \cdot 0.8746 = 1.09\ kg/m^3$$

The dynamic viscosity of HFE7200 vapours can be estimated by knowing the densities of gas and liquid:

$$\mu_{gas} = \mu_{liq} \cdot \frac{\rho_{liq}}{\rho_{gas}} = 13.08\ mPa \cdot s$$

The kinematic viscosity calculated as $\nu_{gas} = \mu_{liq}/\rho$ is:

$$\nu_{gas} = \frac{\mu_{gas}}{\rho} = 0.1879 \cdot 10^{-3}\ m^2/s$$

Thus, the kinematic viscosity of the mixture is:

$$\nu_{mixture} = \nu_{HFE7200} \cdot 0.1254 + \nu_{air} \cdot 0.8746 = 3.96 \cdot 10^{-5}\ m^2/s$$

The values obtained for density and kinematic viscosity can be considered as properties of the gas phase in CFD analyses.

Computation of saturation time

Knowing the percentage of HFE7200 in the gas mixture and having estimated the volume of the pipes in the experimental setup V_{setup} in Appendix A.4.1, it is possible to calculate the relative volume of the HFE vapours.

$$V_{HFE7200-gas} = 0.1254 \cdot V_{setup} = 7.97 \cdot 10^{-5}\ m^3$$

The results obtained on the evaporation rate can be used to estimate the saturation time.

$$t_{sat} = \frac{m_{HFE7200-gas}}{dm/dt}$$

The mass of vapours of HFE7200 in the air is: $m_{HFE7200-gas} = \rho_{HFE7200-gas} \cdot V_{HFE7200-gas} = 0.1236\ g$, thus,

$$t_{sat} = 126\ s \approx 2\ min$$

result in line with the timing of the experiment.

2.7 Database experiment

The data from each experiment are collected in folders named with *"fluid name_ date_ volume used_ initial height difference_ test number"*.

Each test folder is organized as shown in Figure 2.41.

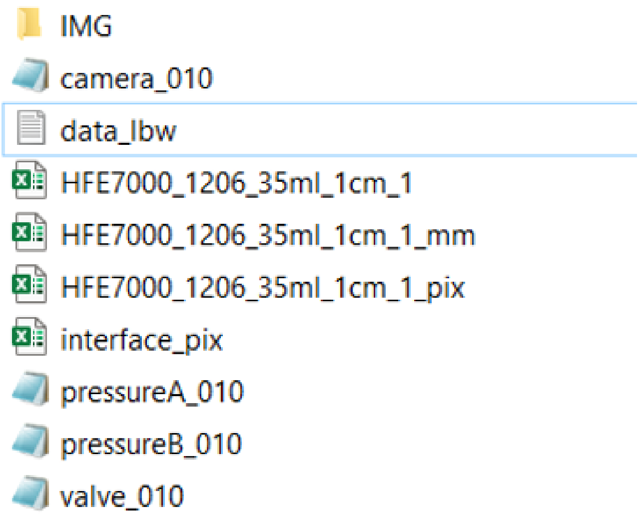

IMG
camera_010
data_lbw
HFE7000_1206_35ml_1cm_1
HFE7000_1206_35ml_1cm_1_mm
HFE7000_1206_35ml_1cm_1_pix
interface_pix
pressureA_010
pressureB_010
valve_010

Figure 2.41: Database folder example

The folder contains

- IMG folder: where there are 700 images of the experiment;
- files.lvm: labview data input of camera voltage, fast opening valve and pressure sensors;
- files.xlsx: Excel file with interface data in mm and pixels in abscissa and ordinate, with optical correction;
- data_lbw.txt: labview data limited to the observation period.

The r_i and h_i data on frame-by-frame interfaces are saved on the four Excel files in different formats and units, two files in mm and two in pixels.

In the "interface_pix" file, the columns represent the coordinates of the surveyed points. The first two columns contain the values r_i and h_i for the first image, and so on for subsequent images.

In the file "HFE7200_1206_4ml_2cm_1", the same information is displayed with the same structure, but expressed in millimeters instead of pixels.

Since the interfaces take different shapes, it is possible that the point pairs (r_i, h_i) detected by the edge detector are different in number for each frame, thus the length of the column pairs is different.

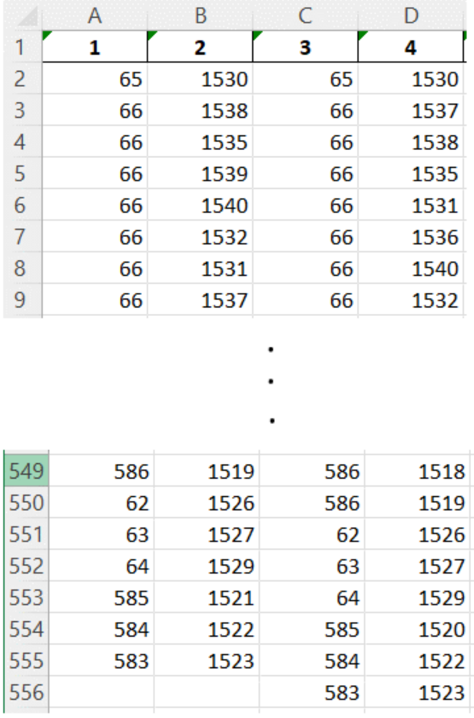

	A	B	C	D
1	1	2	3	4
2	65	1530	65	1530
3	66	1538	66	1537
4	66	1535	66	1538
5	66	1539	66	1535
6	66	1540	66	1531
7	66	1532	66	1536
8	66	1531	66	1540
9	66	1537	66	1532
⋮				
549	586	1519	586	1518
550	62	1526	586	1519
551	63	1527	62	1526
552	64	1529	63	1527
553	585	1521	64	1529
554	584	1522	585	1520
555	583	1523	584	1522
556			583	1523

(a) Database pixel

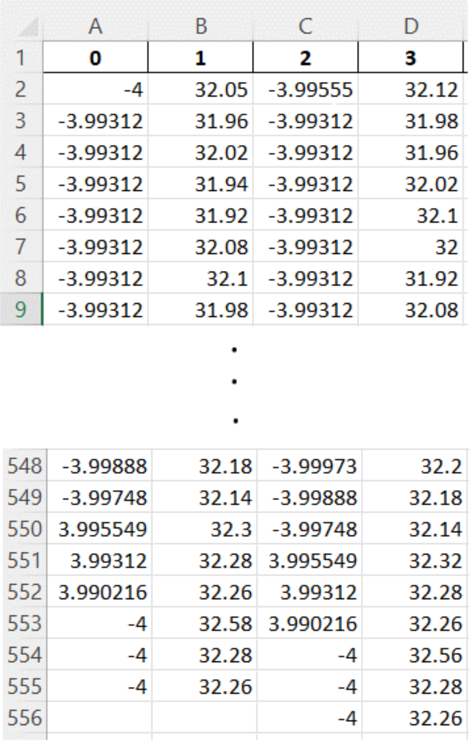

	A	B	C	D
1	0	1	2	3
2	-4	32.05	-3.99555	32.12
3	-3.99312	31.96	-3.99312	31.98
4	-3.99312	32.02	-3.99312	31.96
5	-3.99312	31.94	-3.99312	32.02
6	-3.99312	31.92	-3.99312	32.1
7	-3.99312	32.08	-3.99312	32
8	-3.99312	32.1	-3.99312	31.92
9	-3.99312	31.98	-3.99312	32.08
⋮				
548	-3.99888	32.18	-3.99973	32.2
549	-3.99748	32.14	-3.99888	32.18
550	3.995549	32.3	-3.99748	32.14
551	3.99312	32.28	3.995549	32.32
552	3.990216	32.26	3.99312	32.28
553	-4	32.58	3.990216	32.26
554	-4	32.28	-4	32.56
555	-4	32.26	-4	32.28
556			-4	32.26

(b) Database mm

Among all the x-coordinates of the frames, we created a common abscissa containing the common and non-common elements, and we called it x.

Since for some frames, some x-coordinates do not have the corresponding y-coordinate, not all the column of each image is full.

File "HFE7200_1206_4ml_2cm_1_pix" contains in the first column the x, and in the following columns the respective y-coordinates in pixel. The same applies to file "HFE7200_1206_4ml_2cm_1_mm", but in millimeters.

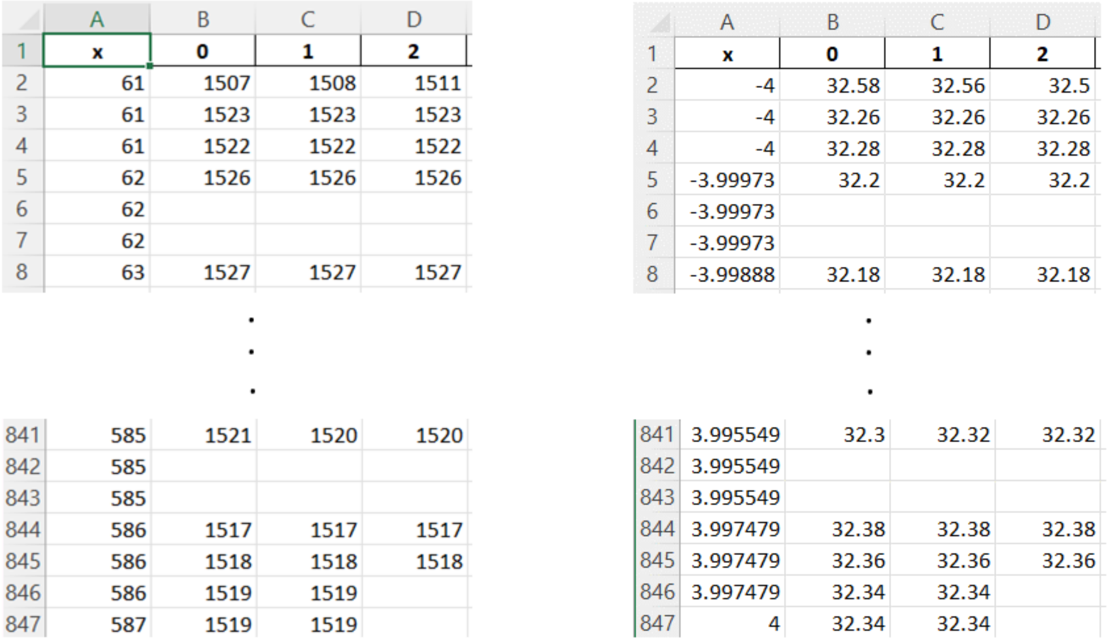

	A	B	C	D
1	**x**	**0**	**1**	**2**
2	61	1507	1508	1511
3	61	1523	1523	1523
4	61	1522	1522	1522
5	62	1526	1526	1526
6	62			
7	62			
8	63	1527	1527	1527
		⋮		
841	585	1521	1520	1520
842	585			
843	585			
844	586	1517	1517	1517
845	586	1518	1518	1518
846	586	1519	1519	
847	587	1519	1519	

	A	B	C	D
1	**x**	**0**	**1**	**2**
2	-4	32.58	32.56	32.5
3	-4	32.26	32.26	32.26
4	-4	32.28	32.28	32.28
5	-3.99973	32.2	32.2	32.2
6	-3.99973			
7	-3.99973			
8	-3.99888	32.18	32.18	32.18
		⋮		
841	3.995549	32.3	32.32	32.32
842	3.995549			
843	3.995549			
844	3.997479	32.38	32.38	32.38
845	3.997479	32.36	32.36	32.36
846	3.997479	32.34	32.34	
847	4	32.34	32.34	

(a) Database pixel

(b) Database mm

Chapter 3

Results

In this chapter, we present the main results obtained from this research.

The description begins with the outcomes achieved on the edge detection of the gas-liquid interface, focusing on HFE7200 and demineralized water and highlighting their differences. In the case of water, the stick-slip phenomenon occurs, which leads to rapid changes from concave to convex shapes, resulting in altered edge detection. This phenomenon does not occur in the case of HFEs.

We employed two fitting models to analyze the different shapes of the interface: one based on physical principles and the other following an empirical approach. We highlight both the results obtained and the restrictions found in the two approaches. The use of interface regression methods aims at finding contact angles and analyzing their behavior as the velocity of the contact line changes.

Tests were also conducted on various liquids, each characterized by different properties, to provide a comparison of their distinct wetting behaviors.

Finally, we present the numerical results obtained through Computational Fluid Dynamics (CFD). We conducted a mesh sensitivity analysis to ensure the accuracy of our results. We also carried out a comparison between the numerical results obtained and the experimental data on HFEs. In addition, we carried out simulations describing the real conditions of the system, exploiting the information obtained through experiments on the evaporation of HFEs.

3.1 Edge detection of moving interface

In this section, we show the main results of edge detection, focusing on HFEs and demineralized water.


(a) $t = 0\ s$ (b) $t = 0.013\ s$ (c) $t = 0.033\ s$ (d) $t = 0.043\ s$ (e) $t = 0.053\ s$ (f) $t = 0.066\ s$ (g) $t = 0.083\ s$

Figure 3.1: Snapshots of the experiment with HFE7200 at several time steps during the interface acceleration.

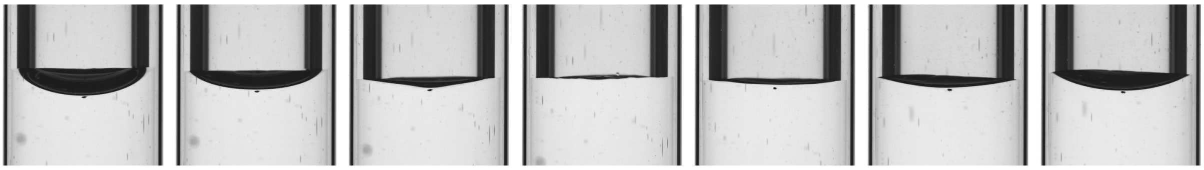
(a) $t = 0\ s$ (b) $t = 0.010\ s$ (c) $t = 0.016\ s$ (d) $t = 0.030\ s$ (e) $t = 0.046\ s$ (f) $t = 0.156\ s$ (g) $t = 0.176\ s$

Figure 3.2: Snapshots of the experiment with demineralized water at several time steps during the interface acceleration and stick slip motion.

An overview of the HFE7200 and demineralized water experiment is shown in Figures 3.1 and 3.2.

The processing of images for the interface detection is explained in Section 2.2 and further elaborated in Appendix A.2.

3.1.1 HFEs edge detection

To show the results obtained by the detector, three different configurations are chosen, one static and two dynamic. These are shown in Fig. 3.3.

The detection of interface shapes is shown in Fig. 3.4. Through these graphs, it is possible to assess the effectiveness of the noise removal function in operating correctly. The image is automatically cropped at the white points, which represent the interface.

(a) Static (b) Dynamic 1 (c) Dynamic 2

Figure 3.3: Experimental tests with HFE7200

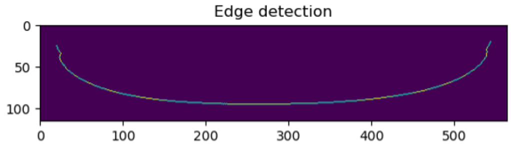

(a) Edge detection static configuration

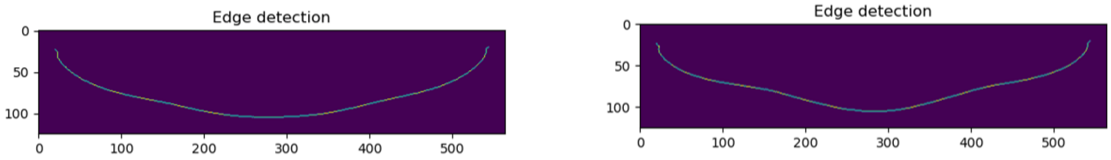

(b) Edge detection dynamic configuration 1 (c) Edge detection dynamic configuration 2

Figure 3.4: Edge detection HFE7200

The effectiveness of edge detection can then be seen in the detail of Fig. 3.5, which shows the detected points superimposed on the original image.

Figure 3.5: Detail interface detection

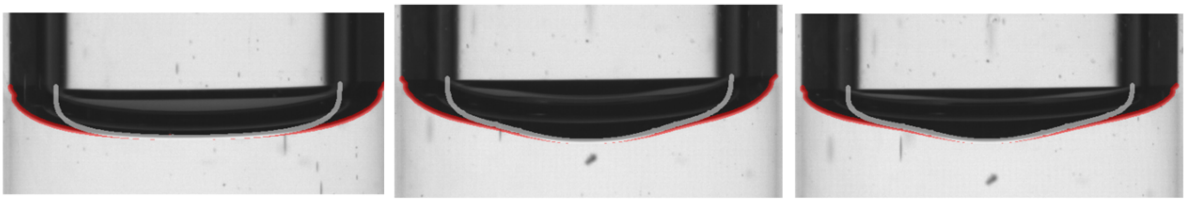

Figure 3.6: Detail optical correction

After the optical correction described in Section 2.2.1, the gas-liquid interface is obtained. A detail of optical correction is shown in Fig. 3.6.

The detection process for the HFE7000 is similar. the only change is the refractive index.

3.1.2 Demineralized Water edge detection

The operating principle of the detector in the case of tests on demineralised water is the same as for HFEs, but with some modifications to consider.

The main difference of the experiment with demineralized water consists in the change of shape of the interface from concave to convex. In practice, for a concave interface the shape of the interface results from the light deviation due to the gas phase spherical cap at the meniscus height, the liquid phase at the interface appears with a bright color. In the case of a convex interface, the shape of the interface results from the light deviated by a spherical cap of liquid, hence the liquid phase at the interface results with the darkest color.

Two comparison tests are shown in Fig. 3.7 and 3.8. It must be noted that the optical distortion differs in the two cases due to the different refractive indexes involved. In the first case, the light is deflected by the water, while in the second case, light passes only through the quartz.

Figure 3.7: Test Demineralized Water

Figure 3.8: Test Demineralized Water

The sudden change of convexity of the interface is due to the pinning phenomenon, discussed in more detail in the following section.

The two interfaces are shown in Fig. 3.9.

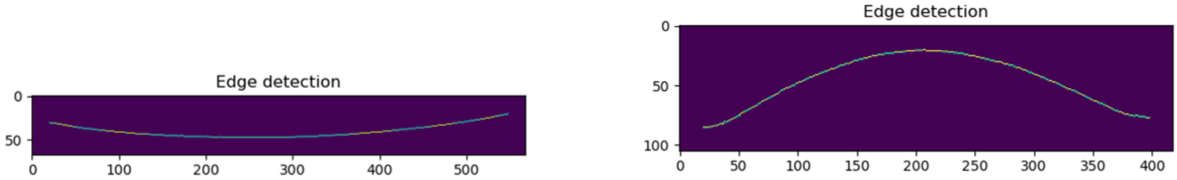

(a) Water edge detection 1

(b) Water edge detection 2

Figure 3.9: Water edge detection

In the case of Fig. 3.9b, the interface can only be detected between the inner edges.

3.2 Fluids comparison

We tested six different liquids during the experimental campaign, whose properties at room conditions are shown in Table 3.1. The static image of each test is shown in Fig. 3.10.

		HFE7200	HFE7000	Dem. water	Isopropanol	Ethanol	Diprop. Glycol
Density (ρ)	kg/m^3	1423	1404	997	785	789	1020
Dynamic viscosity (μ)	$mPa\ s$	0.64	0.49	0.97	2.46	1.20	75.00
Surface tension (σ)	mN/m	13.62	12.33	72.01	21.70	22.39	35.00
Refractive index		1.28	1.26	1.33	1.38	1.36	1.44

Table 3.1: Fluid physical properties at 298 K

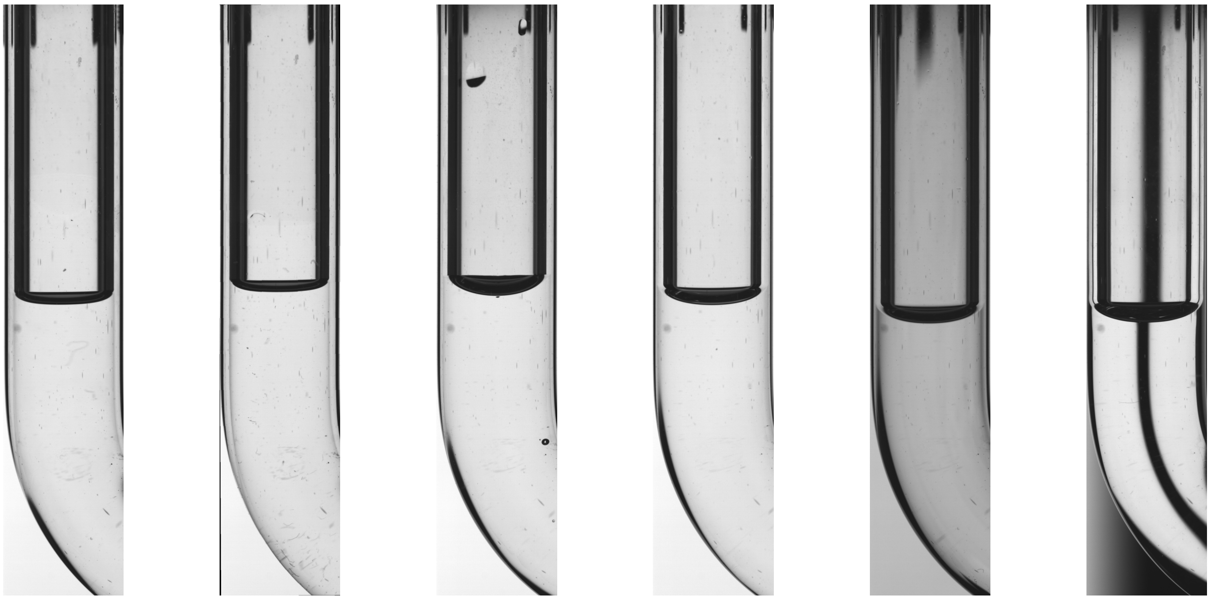
(a) HFE7200 (b) HFE7000 (c) Demineralized Water (d) Isopropanol (e) Ethanol (f) Dipropylene Glycol

Figure 3.10: Experimental tests with different liquids

The HFEs exhibit high volatility, as seen in Section 2.6, and low surface tension. Comparing HFE7200 and HFE7000, the first demonstrates higher dampening due to its elevated dynamic viscosity.

Among the tested liquids, demineralized water showcases the highest surface tension. The phenomena observed are pinning and contact angle, the latter ranging from 90° to 180°. Pinning arises from the interplay of two factors: the tube's surface roughness and the polar nature of water, leading to electrostatic effects [26].

Furthermore, the study examines isopropanol and ethanol, both known for their low density. These liquids find extensive employment in microfluidics applications.

Concluding the lineup is dypropylene glycol, characterized by its notably high dynamic viscosity. This viscosity attribute eliminates oscillations during the experiments. This particular liquid finds widespread use in coating applications due to its viscosity properties.

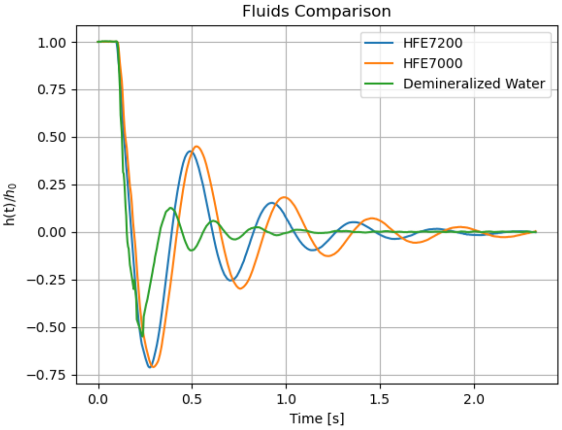

Figure 3.11: Comparison between HFEs and Demineralized Water

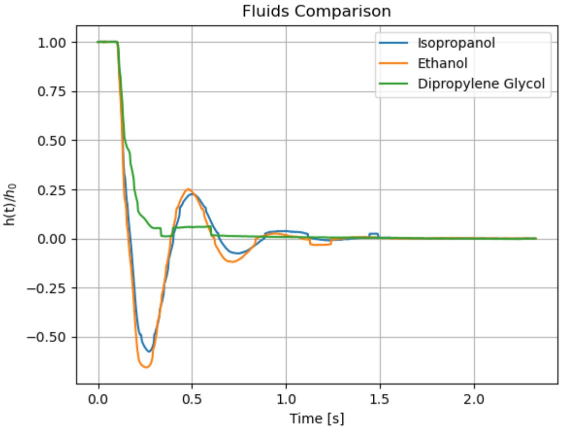

Figure 3.12: Comparison between Isopropanol, Ethanol and Diprop. Glycol

The comparative graph of all the fluids used is in the Appendix B.1.

As can be seen in Fig. 3.11, where the evolution of the interface over time is shown, HFEs oscillate more than other liquids.

Dipropylene glycol, a very viscous fluid, does not oscillate but reaches equilibrium condition in about ≈ 0.5 seconds.

In the image from the dipropylene glycol test 3.10f, the presence of a disturbance in the central region of the image is evident. Due to the refractive index, the interface was not visible, so a two-lamp setup shown in Fig. 3.13, was used in order to obtain a better visualization of the interface.

The resulting image shows a clearer and more defined interface. However, it should be noted that this optimization resulted in a reduced visibility of the central part of the object under investigation.

Figure 3.13: Dipropylene glycol test with two LED lamps

3.3 Interface Modeling

Based on what was described in the section 2.4, we processed the experimental images using two models. The first model uses the Meniscus Profile Method (MPM), which is based on an optimization process from an analytical formulation of the interface. This method uses the contact angle θ as an optimization parameter. The second model, Support Linear Regression (SVR), on the other hand, is an empirical model, whereby the contact angle must be found analytically.

3.3.1 Inertial-less model

The inertial-less model describes static or quasi-static interface behavior. It is a physical model, based on the balance of gravitational and capillary forces.

We present in Figures 3.14 and 3.15 two cases of the test performed with the HFE7200, one of a static interface and the other of a dynamic interface.

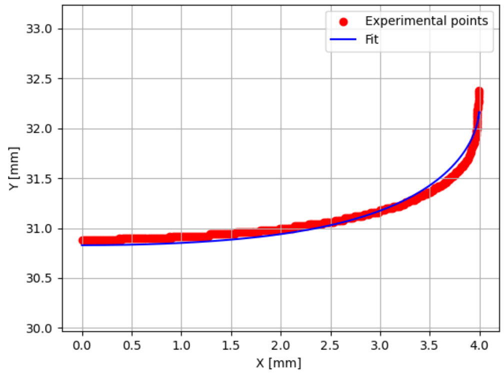

Figure 3.14: ILM static

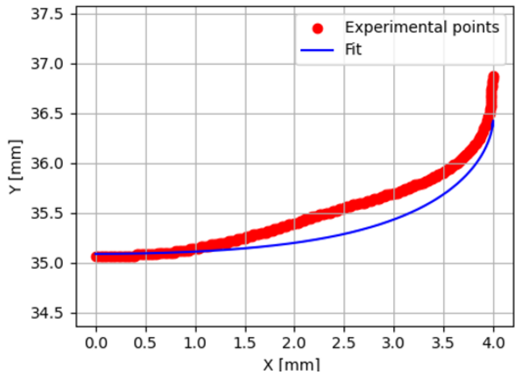

Figure 3.15: ILM dynamic

Since the inertial-less model is essentially a quasi-static model, thus suitable for representing situations where the interfaces are stationary or moving at low speeds, it can be seen that this model effectively fits the case illustrated in Fig. 3.14. In this case, the contact angle has been measured as $\theta_{st} = 1.093\ deg$.

On the other hand, in Fig. 3.15, a dynamic case is examined. In this situation, the contact angle turns out to be $\theta_{dyn} = 0.937°$.

However, the viscous forces that arise with velocity do not intervene in the presented model 2.15, and therefore it is not reliable for dynamic interfaces.

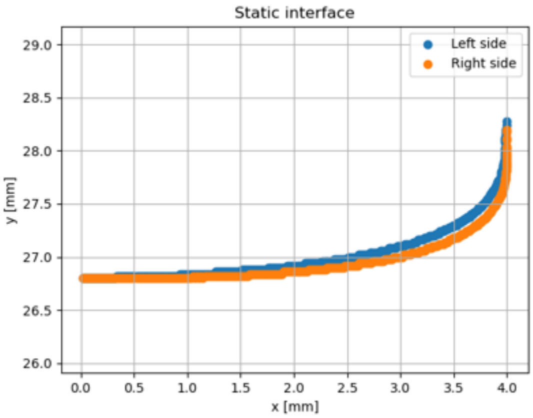

(a) Symmetry of static interface

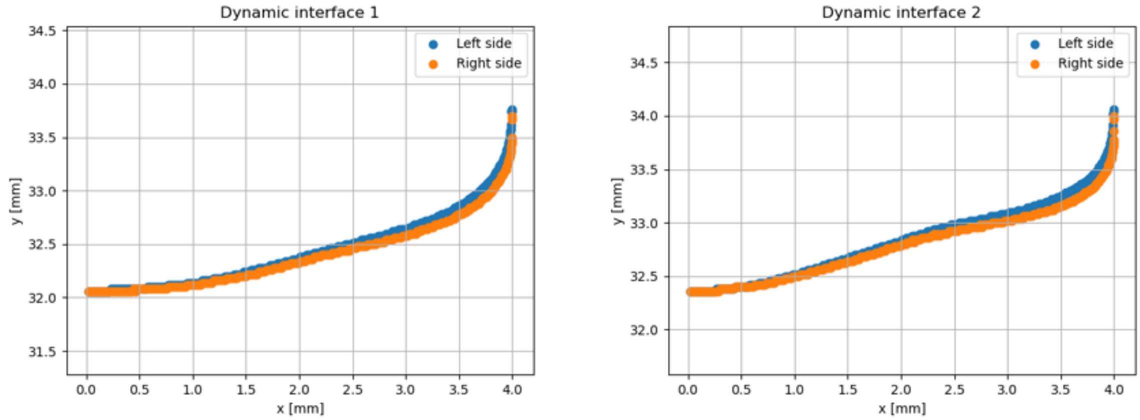

(b) Symmetry of dynamic interface 1

(c) Symmetry of dynamic interface 2

The limitation of this model, apart from the fact that it is quasi-static, is that it applies to symmetrical interfaces. An examination of the symmetry of the shapes obtained shows that, even for the static case in Fig. 3.16a, this requirement is not fully guaranteed. In the three cases, the two sides of the interface differ in percentage terms by 0.20% in the case of the static interface, 0.08%, and 0.15% in the case of the two dynamic interfaces. The difference in symmetry between the two sides could be attributable to small misalignments in the experimental setup or, possibly, in the position of the camera, although all details of the setup were carefully checked.

3.3.2 Support vector regression

In the case of the Support Vector Regression, we analyzed the same two cases seen above, a static interface and a dynamic one.

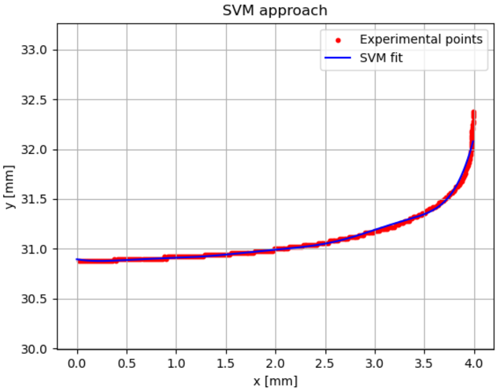

Figure 3.17: SVM static

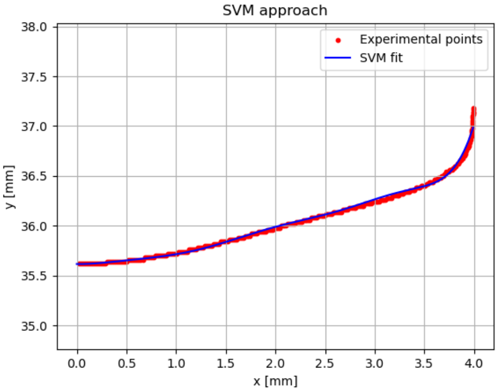

Figure 3.18: SVM dynamic

In Figure 3.17, we can observe the static case, in which the contact angle is equal to $\theta_{st} = 15.096\ deg$. In Figure 3.18, on the other hand, we can see the dynamic case, in which we obtain a satisfactory result with a contact angle of $\theta_{dyn} = 15.935\ deg$.

The results obtained from both methods highlight the need to develop a model capable of accurately reproducing dynamic interfaces. In the static case, a good description was obtained, although the contact angle results showed discrepancies, attributable to the different calculation methods used in the two models.

Currently, for the dynamic case, the only approach that has proved reliable is based on Support Vector Regression (SVR).

With this method, being a regression of experimental data, the contact angle is found by calculating the tangent of the last point of the fit, as shown in Fig. 3.19.

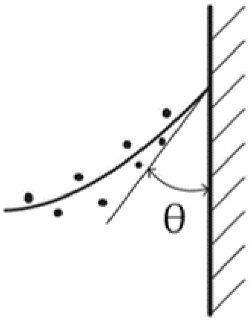

Figure 3.19: Detection contact angle

3.3.3 Contact line behaviour

In most cases, the dynamic contact angle θ and the velocity of the contact line u_{cl} are linked by the constitutive law shown in Fig. 3.20.

The constitutive law, showing the traditional contact line behavior, can be obtained by the tilted plate method, in which the speed can be controlled by tilting the surface at different angles. As discussed in the introductory Chapter 1, when the velocity of the contact line is zero, i.e. $u_{cl} = 0$, a phenomenon known as wetting hysteresis occurs. The wetting hysteresis describes the difference between the advancing contact angle and the receding contact angle on an inclined surface before the contact line is set into motion.

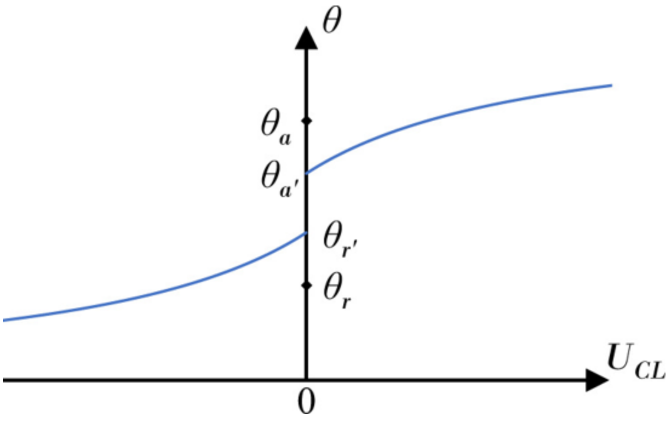

Figure 3.20: Traditional contact line behaviour [13]

Contrary to the previously described case, the experiment conducted using the U-shaped tube is particularly useful for examining how the velocity of the contact line affects the dynamic contact angle. However, it is important to note that due to the oscillating nature of the liquid in this experiment, it is not possible to control the velocity of the contact line continuously, as can be done in the tilted base experiment.

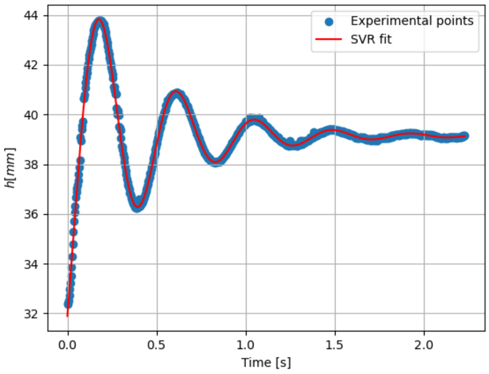

Figure 3.21: Contact line position, fitted with SVR

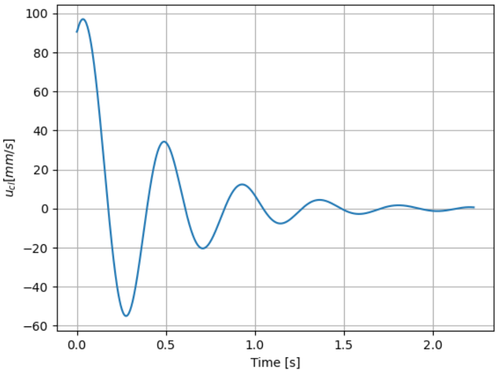

Figure 3.22: Contact line velocity

In the case of the U-shaped tube, the velocity of the contact line oscillates over time, as shown in Figure 3.22. This implies that the graph linking θ to u_{cl} moves from right to left in several steps, given the oscillating characteristic of the velocity.

It is important to emphasize that contact angle hysteresis may not be observable in this experiment as the continuous oscillation of the liquid prevents the contact from stabilizing in a specific state for a prolonged period. However, it should be noted that in the case of demineralized water, for example, when the contact line pins, a range of contact angles can be observed for which hysteresis can be computed. It could be assumed that the fact that hysteresis is not observed with HFE could simply be due to the fact that HFE does not have a wide enough hysteresis range to be observed. This statement is also confirmed by the fact that pinning is not observed in experiments with HFEs.

Using the contact angle results obtained with SVR in Section 3.3.2, it is then possible to reproduce the contact line behavior.

The Davis-Hocking correlation simply links the contact angle θ with the contact line velocity u_{cl} via the mobility parameter M [27], such as:

$$M\theta = u_{cl} \tag{3.1}$$

In Fig. 3.23, a comparison between the experimental results and the Davis-Hocking correlation can be observed. The analysis of the experimental data clearly shows that as the capillary number increases, and therefore at higher velocities, the contact angle θ increases. On the contrary, at low velocities, the contact angle assumes lower values, following a behavior in line with traditional expectations.

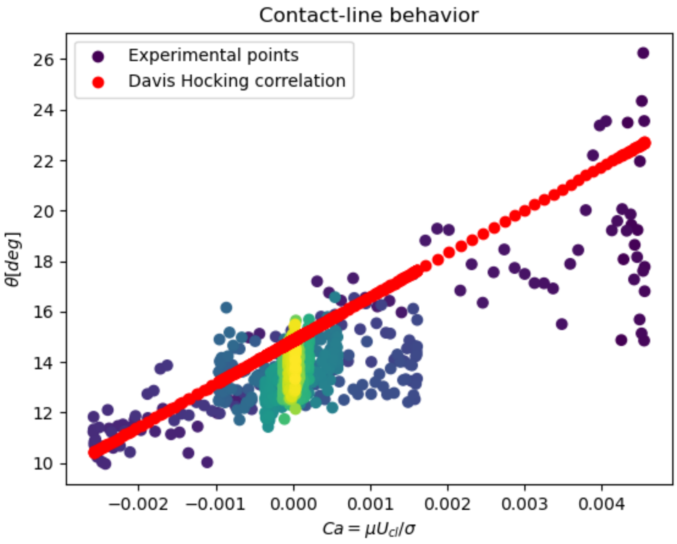

Figure 3.23: Davis Hocking correlation

3.4 CFD Results

In an attempt to understand how CFD is a reliable methodology for understanding real phenomena, this section brings together a series of simulations.

It starts with an analysis of the sensitivity of the mesh and then moves on to a comparison of the results obtained through CFD and those from experiments. In addition, comparisons are made between HFEs.

Finally, the impact of oscillations when using a mixture of HFE and air instead of pure air is examined. The section concludes with a detailed analysis of the velocity field and interface morphology.

3.4.1 Mesh sensitivity

Starting from a basic mesh, two further meshes are proposed, one coarser and one denser, in order to study the sensitivity mesh of the problem under investigation.

The coarser mesh was obtained by multiplying the mesh parameters by 11/10, from a number of elements of 73800 to a number of elements of 58464.

On the other hand, the denser mesh has 839040 elements because the radial resolution has been multiplied by 2/15, and the other parameters have been halved.

The three meshes are shown in the Fig. 3.24.

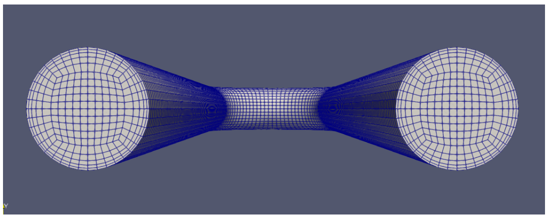

(a) Base mesh

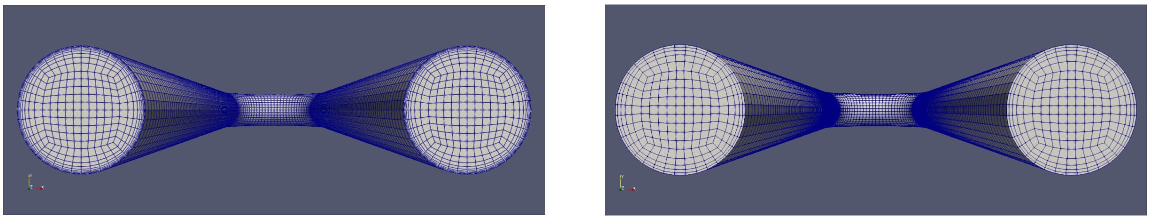

(b) Fine mesh

(c) Coarse mesh

Figure 3.24: Mesh used for the study of mesh sensitivity

The graph in Fig. 3.25 shows the behavior over time of the midpoint of one of the sides of the tube. The results show that there are no significant differences between the three meshes considered. In fact, it is observed that the time course is almost identical for both the basic and the densest configurations. From this, it can be deduced that increasing the density of elements in the mesh does not lead to an improvement in the solution but rather results in an increase in the number of discrete elements and, consequently, an extension of the time required for resolution.

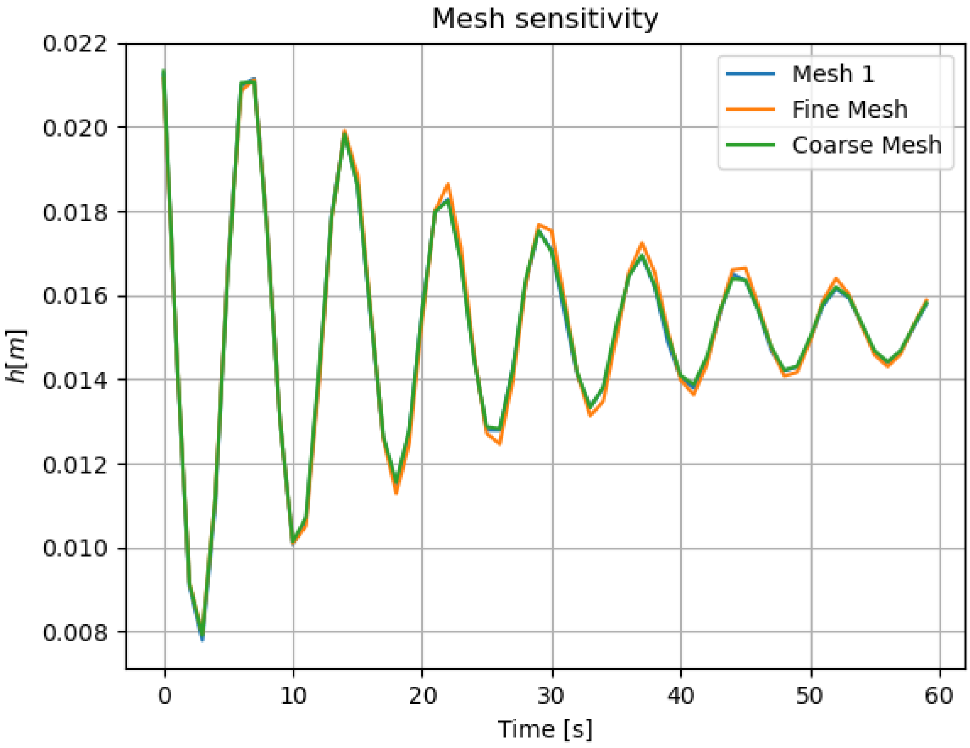

Figure 3.25: Mesh sensitivity analysis

3.4.2 CFD vs Experiments

A comparison between the CFD numerical simulation and physical experiments is then proposed in terms of the relative oscillation in time, expressed as the h/h_0 ratio.

The reference experiment involves a volume of 4 ml of liquid HFE7200, with an initial height difference of 2 cm between the columns of liquid in the two sides of the tube. In this comparison, experimental test results were considered together with those derived from two numerical simulations using different computational grids.

As previously noted, the two meshes appear to be similar, there is no real improvement by using a finer mesh.

More relevant is the comparison between the experimental results and those obtained through CFD. An analysis of Fig. 3.26 clearly shows that the oscillations found in the experiment are significantly more damped than those resulting from the CFD simulations. This disparity can be attributed to several factors. Firstly, CFD, in its current model, does not adequately account for the interaction between the fluid and the wall surface. This represents an inherent limitation in current simulation models, which could lead to an overestimation of oscillations compared to experimental reality.

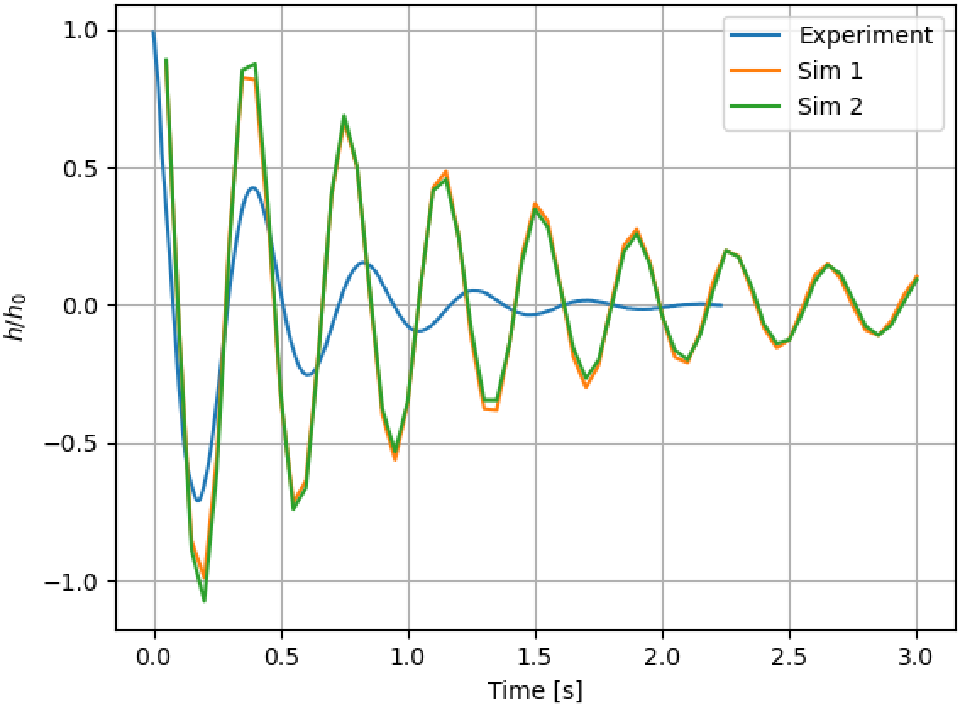

Figure 3.26: Experiments vs CFD simulations

Secondly, it is important to note that both liquid and gas are considered in multiphase simulations. However, the gas was always considered as air. In reality, in cases of highly volatile substances such as HFEs, the gas present above the liquid may be a mixture of air and vapours from the liquid itself. This diverse gas composition could lead to a significant discrepancy in the results compared to the actual experimental environment.

It can also be seen that while there is initial agreement in the oscillation period during the first cycle, this agreement dissipates as subsequent oscillations occur.

The loss of coherence over the period could have several causes, including the presence of damping forces, such as viscous forces, or a loss of volume due to evaporation of the HFE.

During the experimental setup phase, it was verified that there was no loss, however, due to the large number of instruments used, this possibility cannot be completely excluded.

3.4.3 HFEs comparison

One notable result concerns the comparison of two HFE fluids, the HFE7200 and the HFE7000. Analyzing the properties shown in the table 3.1, a significant difference in density, dynamic viscosity, and surface density emerges between the two.
Interestingly, HFE7000 has a lower viscosity than HFE7200. This has a direct impact on the behavior of oscillations within fluids, as demonstrated experimentally. The lower viscosity of the HFE7000 implies a lower damping capacity of the oscillations, which results in larger oscillatory amplitudes, as reported in the experimental data.

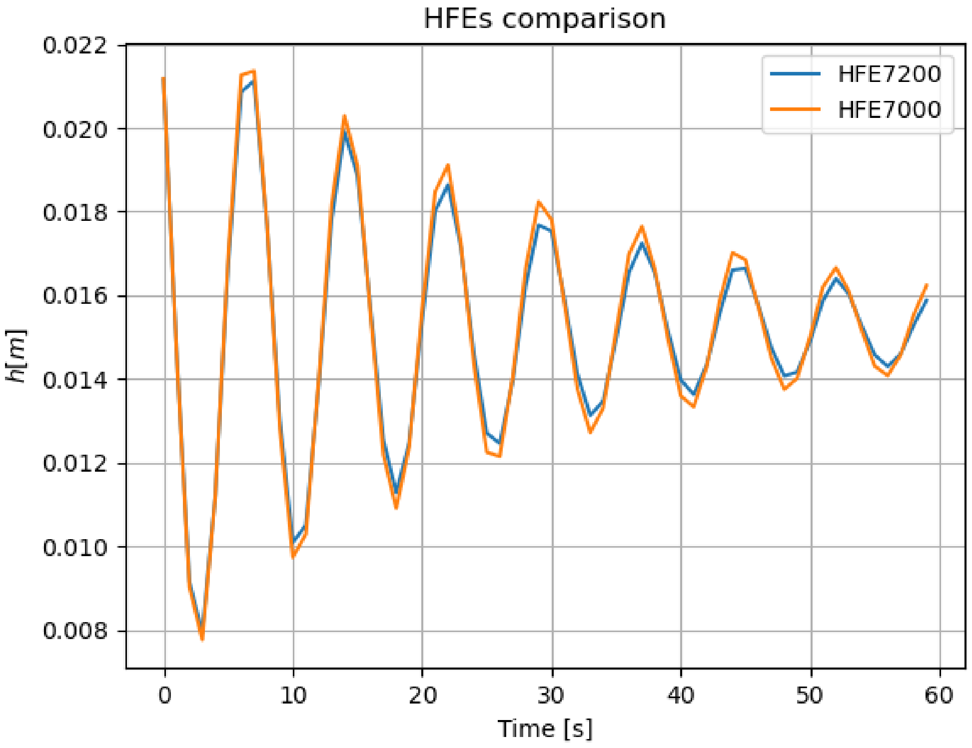

Figure 3.27: HFEs comparison - CFD results

Comparing the numerical results in Fig. 3.27 with the experimental results in Fig. 3.28, it can be seen in both cases that the HFE7000 has larger oscillations. This is due to the lower viscosity compared to the HFE7200. In the case of the CFD simulation, the period remains the same, as the volume involved does not change. As mentioned in the previous section, the experimental case may be subject to volume changes due to evaporation, or an initial volume difference for the two cases.

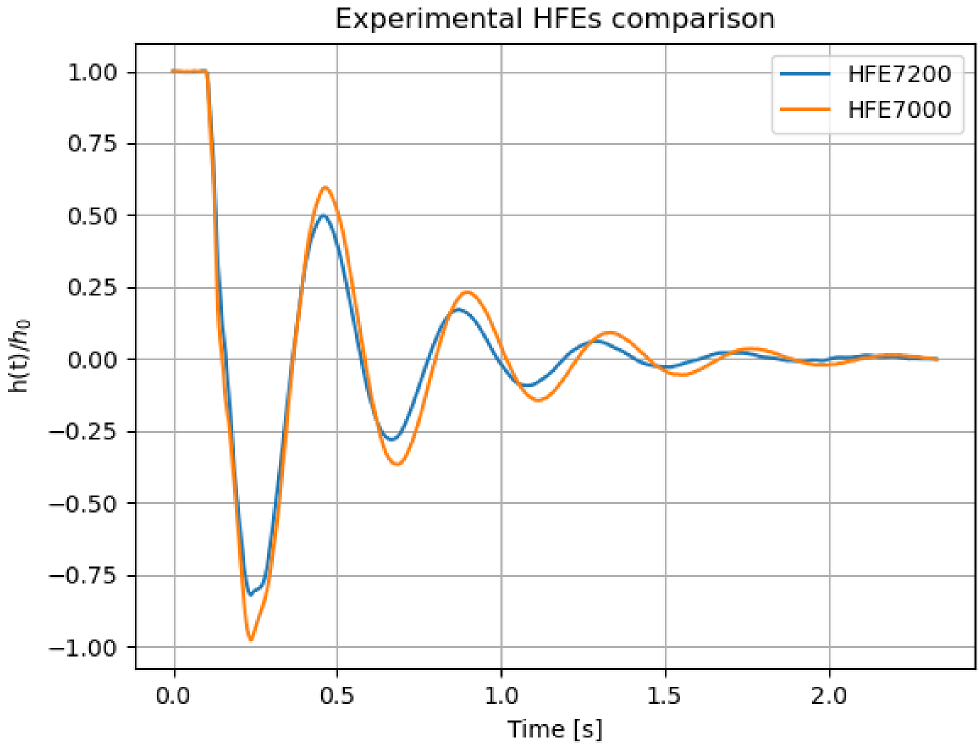

Figure 3.28: HFEs comparison - Experimental results

3.4.4 Experiment with a gas mixture of air and HFE vapours

The numerical simulations conducted simplified reality by considering the use of HFE as liquid and air as gas in the multiphase problem. However, in real experiments, HFE tends to evaporate in the pre-test phase and saturates the experimental setup volume. Thus the gaseous phase in the experiment is a gaseous mixture of air and HFE vapour.
Since the experiments were carried out under saturation conditions, it was useful to make a preliminary study of the evaporation of HFEs, in Section 2.6.
Assuming working in a fully saturated condition, the test case consists of HFE72000 as liquid and a mixture of air and HFE7200 vapours gas. To perform this simulation in the Open Foam environment, it is necessary to know the density and kinematic viscosity of the gas, estimated in the section 2.6.
Such a study is useful for representing a simulation of a case that is closer to experimental reality. On the other hand, it helps us to understand how and if the dynamics of the

experiment change.

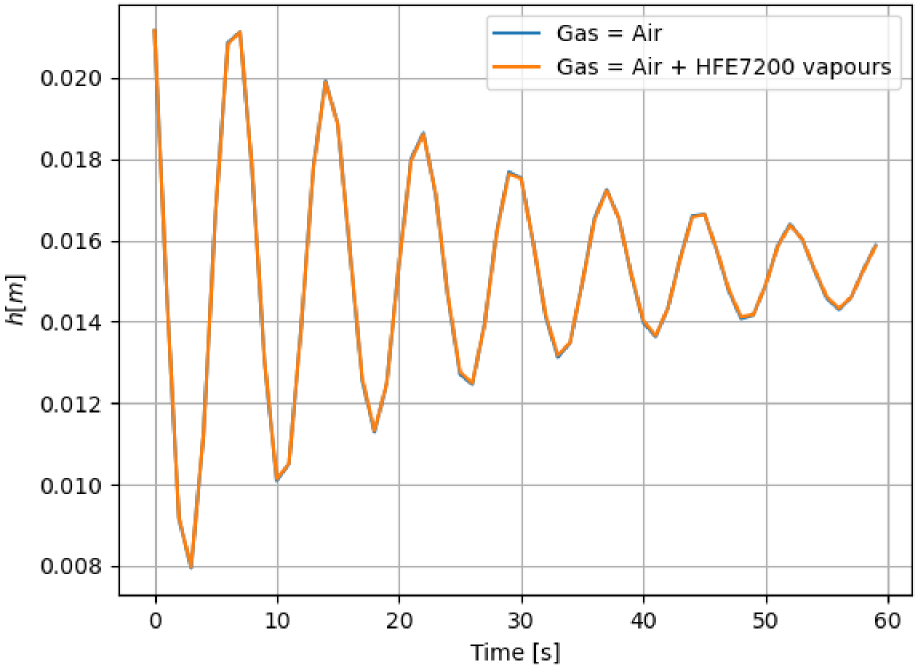

Figure 3.29: Comparisono between HFE7200 + Air and HFE7200 + Gaseous mixture of air and vapours of HFE7200

The analysis performed, as can be seen in Fig. 3.29, shows that the change in the physical properties of the gas does not affect the oscillations in time.

3.4.5 Velocity analysis

An analysis of the velocity field inside the U-shaped tube is proposed. This research focuses on the observation of the velocity field in the numerical results, with the aim of confirming the common assumption of a Poiseuille flow in a vertical channel, which has already been experimentally verified using the Particle Image Velocimetry PIV technique by Fiorini et al. [28], in a U-shaped tube experimental setup.

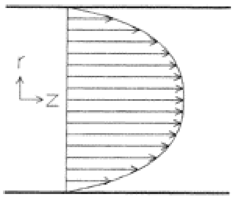

Figure 3.30: Poiseuille profile

Four different configurations are investigated by analyzing the velocity field. We observe side B of the tube, as shown in Figure 3.31.

The four images are characterized by the behavior of the liquid at the wall, which has a lower speed. This indicates the typical Poiseuille velocity profile.

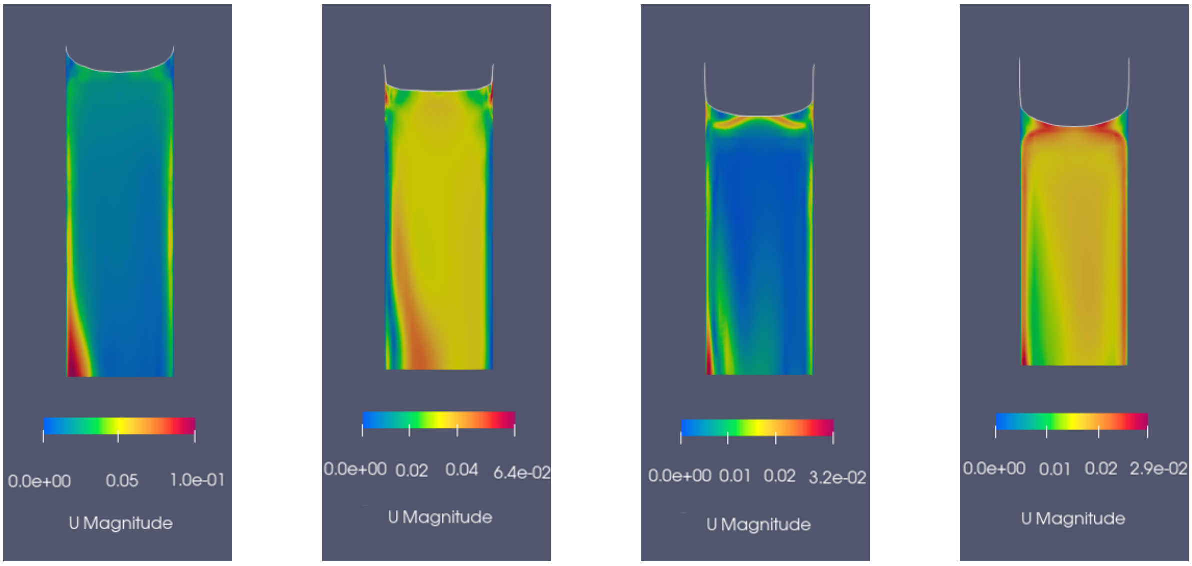

(a) $t = 0.2\ s$ (b) $t = 0.55\ s$ (c) $t = 0.95\ s$ (d) $t = 1.35\ s$

Figure 3.31: Velocity field of the side B of the U-shaped tube

In Fig. 3.32, the velocity field in two different sections for four time steps.

In Fig. 3.32c the speed is flat. At time $t = 0.95\ s$ there is in fact a change of direction in the oscillation, so the velocity is almost zero.

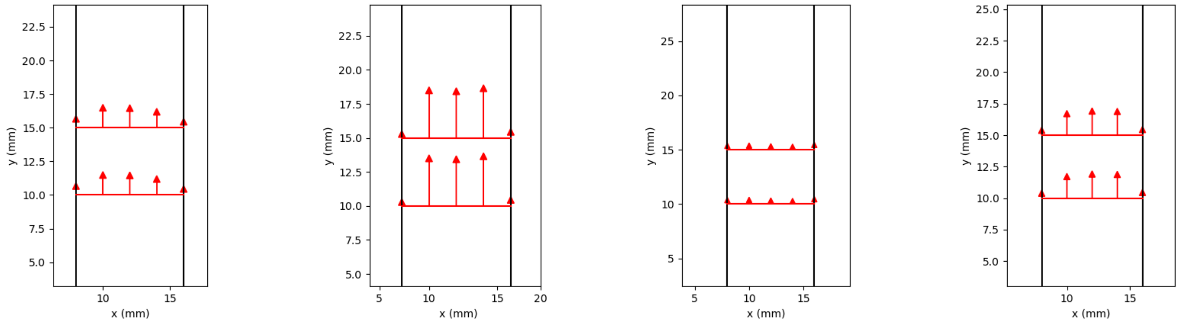

(a) $t = 0.2\ s$ (b) $t = 0.55\ s$ (c) $t = 0.95\ s$ (d) $t = 1.35\ s$

Figure 3.32: Velocity field inside the tube

Up to a certain distance from the liquid-gas interface, the velocity field is dominated by Poiseuille flow, while below this the velocity profile flattens out and radial velocity components appear.

Chapter 4

Conclusions and future works

The main objectives of this research were to extend the understanding of the wetting behavior of cryogenic propellants and to create a large database of experimental data to validate predictive models. These objectives are essential for the handling of space propellants in a gravity-free environment.

To achieve these objectives, experiments were conducted using two quasi-capillary U-shaped tubes, where oscillations were induced in the liquid column in response to a change in pressure on either side. These experiments used high-speed cameras and back-light configurations to record the movement and deformation of the gas-liquid interface. We analyzed different types of fluids, covering a wide range of viscosities and surface tensions. Particular attention was paid to the fluids HFE7000 and HFE7200, which are used as models for space propellants. It was found that these fluids exhibit significantly different wetting behavior than demineralized water. The dynamics of the contact line are very similar for HFEs, whereas it is different for demineralized water, which pins multiple times.

We used the indirect Meniscus Profile Method (MPM), based on the inertial-less model, to describe the liquid-gas interface. This model proved effective in accurately approximating static or quasi-static interfaces but showed limitations in modeling the particular shapes of moving interfaces.

To address this challenge in the future, we could consider adopting the "inertia-corrected" model developed by Fiorini et al. [19]. This model could provide a better representation of dynamic interfaces and could be subject to further improvement.

We also used the Support Vector Regression (SVR) technique to obtain a regression of both static and dynamic interfaces. This method proved effective in modeling the interfaces accurately. However, the contact angle is calculated by using the tangent to the wall of the last point of the fitting curve. It is important to note that this approach can lead to overestimating the contact angle compared to those obtained using the MPM method. We carried out numerical simulations using Computational Fluid Dynamics (CFD) and the Volume of Fluid (VoF) without interface reconstruction, to compare simulation results with experimental data. This comparison revealed that capillary effects are still inadequately modeled in CFD solvers, which currently only consider fluid hydrodynamics. More extensive research is required to enhance the precision of numerical models in CFD solvers.

Since the contact angle varies depending on the gas present above the liquid, future work will focus on analyzing the contact angle under single-species conditions. Our experimental setup will be modified to ensure complete isolation by creating a vacuum environment inside the pipes using a pump. In this way, the HFE will gradually begin to evaporate until the experimental volumes are completely saturated, resulting in a system containing only HFE in the liquid and gas phases.

A possible solution for the experimental setup is shown in Figures 4.1 and 4.2.

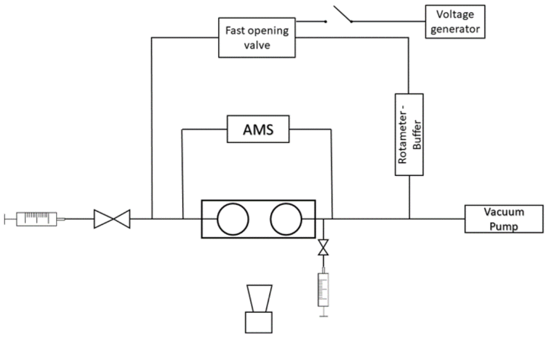

Figure 4.1: Diagram of the single-species setup

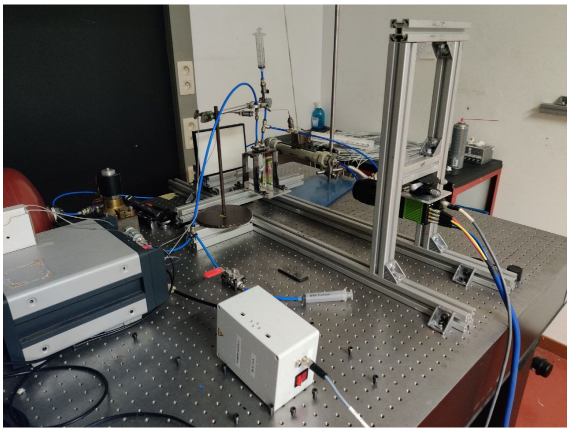

Figure 4.2: Experimental setup

In conclusion, this research has made important contributions to the understanding of wetting dynamics in capillary flows, particularly in cryogenic propellants used in space. The experimental results demonstrated significant variations in wetting behavior between different fluids and highlighted challenges in the numerical modeling of such phenomena. These results may have significant implications for the design and management of space propellants in microgravity conditions. Further research is needed to develop more accurate numerical models that account for capillary effects more fully in CFD solvers.

Appendix A

Methodology

A.1 Plate project

In order to hold the structure and to be able to insulate it from the outside, a plate with a slot and two sealing plates drilled in the centre with a GAZ 1/4" hole are required. The plates were made by the VKI production department. They are made of aluminium and drilled with M4 threaded holes. At the base of the plate with the slot there is a layer

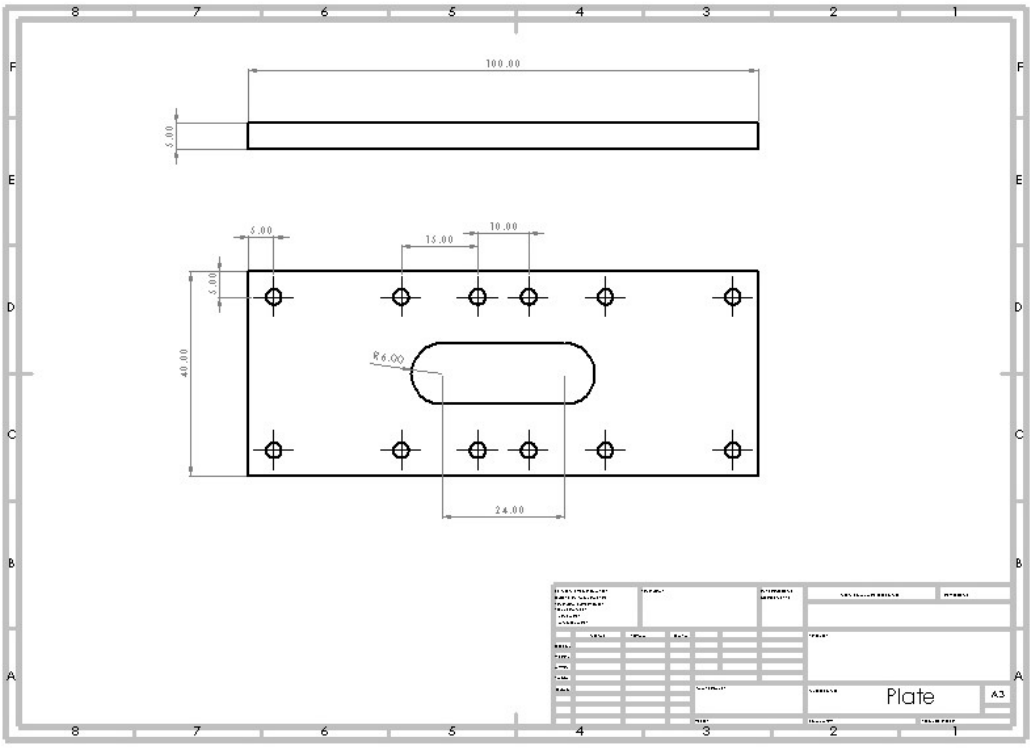

Figure A.1: Plate project

of rubber to avoid bringing the quartz into contact with the aluminium.

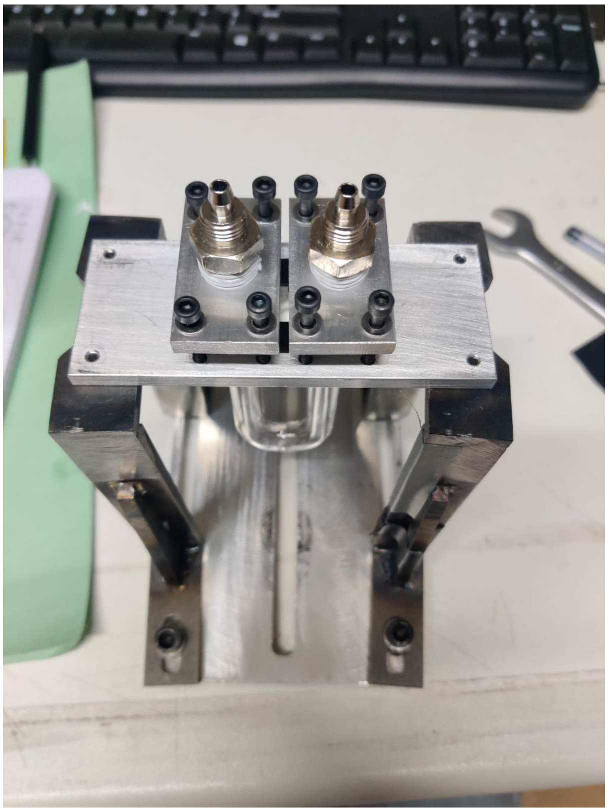

Figure A.2: Plate

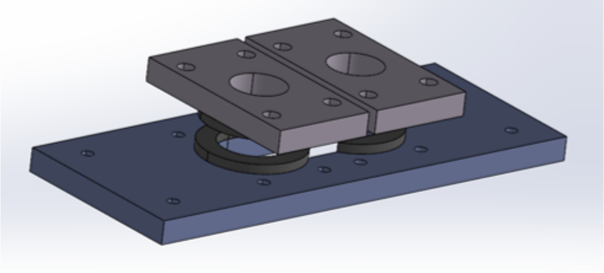

Figure A.3: Plates

A.2 Image analysis

A Python script *generate_ database* was created for the analysis of the images.

generate_database

Description

This script performs image processing and data analysis tasks on a series of experimental images. The script includes several functions that manipulate images, detect edges, clean images, crop images, and extract relevant data. It also provides a user interface for selecting input parameters and directories.

Functions:

- `print_img(image, tit)`: Displays an image with a given title using matplotlib.
- `read_dig_img(filename)`: Reads and modifies an experimental image, enhancing the edges and converting it to a digitized form.
- `detect_edge(forma, left_crop, right_crop)`: Detects and draws the contours at the border between black and white in an image, allowing further cleaning.
- `clean_image(img)`: Cleans the image by dividing it into bands and removing deviating bands based on white pixel count.
- `cropimg(grad_img3)`: Crops an image by finding the white elements and adjusting the cropping box accordingly.
- `find_lowest_white_pixel_row(image)`: Finds the row with the lowest white pixel in the image.
- `select_directory(tit)`: Opens a file dialog to select a directory and returns the selected path.
- `select_csv_file()`: Opens a file dialog to select a CSV file and returns the selected file path.
- `main()`: The main function that executes the image processing and data analysis tasks. It prompts the user for input values, selects a directory, processes each image, saves relevant data to a CSV file, and displays cropped images.

Execution: The script prompts the user to enter values for left and right cropping. It then asks the user to select a folder containing the experimental images. After processing each image, the script saves the extracted data to a CSV file and displays the cropped images. The runtime of the script is recorded and displayed at the end.

The script provides a comprehensive image processing and data analysis pipeline, allowing researchers to analyze experimental images efficiently.

Below are the processing steps for the two dynamic cases.

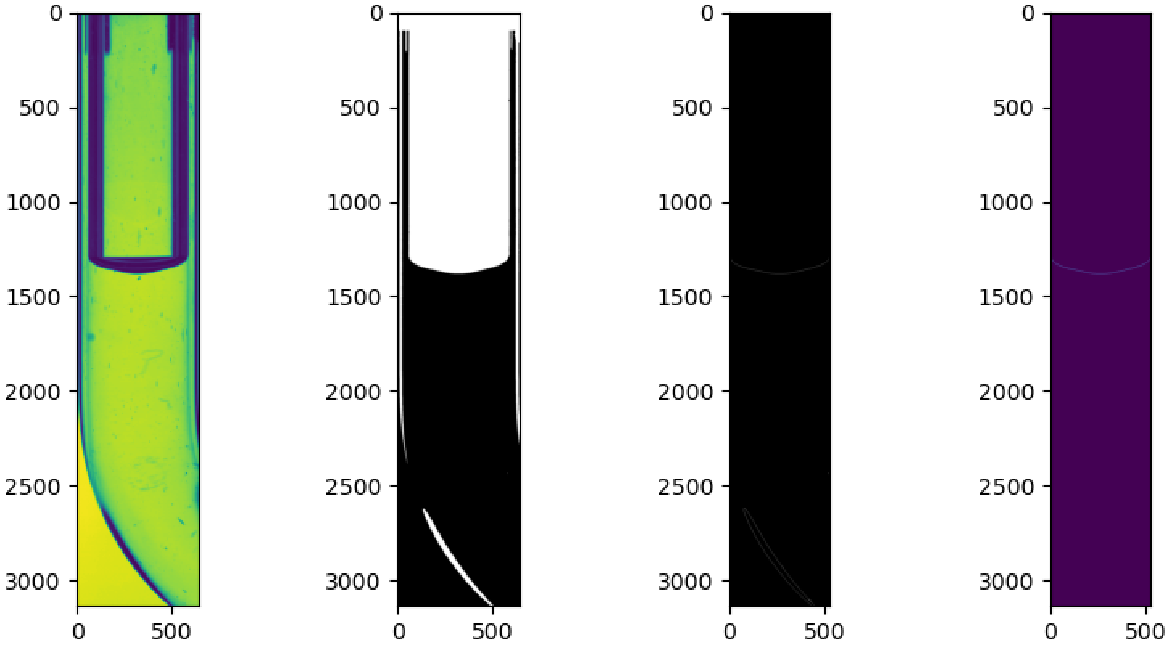

(a) Step 1 (b) Step 2 (c) Step 3 (d) Step 4

Figure A.4: Edge detection process

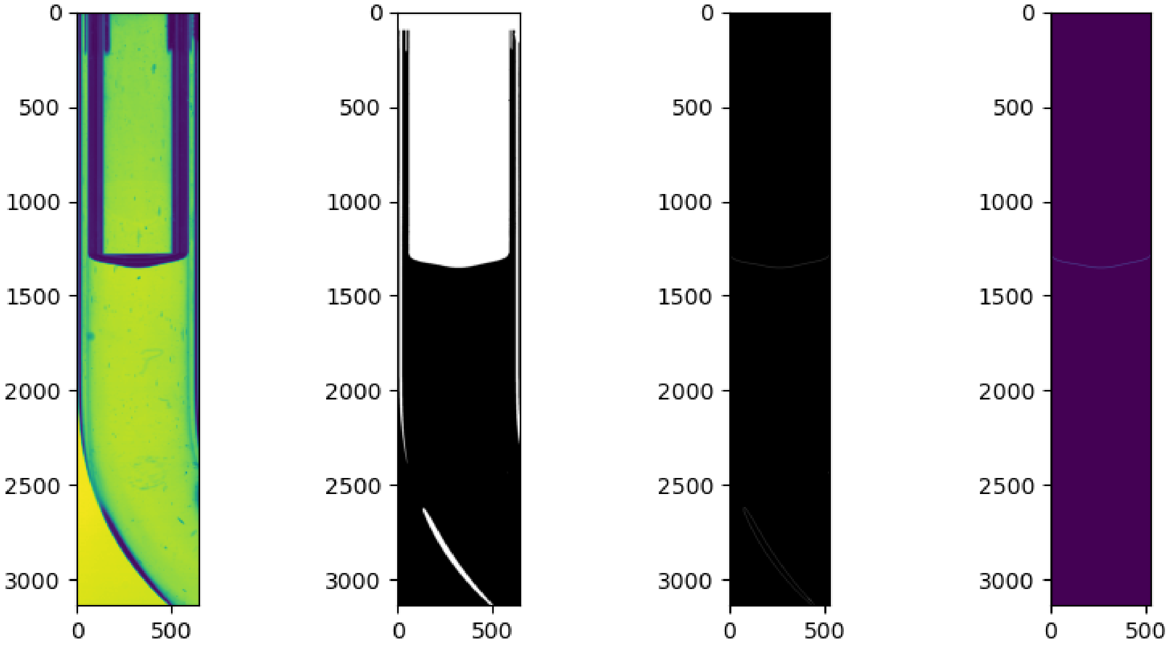

(a) Step 1 (b) Step 2 (c) Step 3 (d) Step 4

Figure A.5: Edge detection process

A.3 Properties of HFEs

For the experiments conducted, the fluids used were HFE7000 (C3F7OCH3) and HFE7200 (C4F9OCH3). These fluids are refrigerants with relatively low normal boiling points (34 °C for HFE7000 and 40 °C for HFE7200), making them suitable for conducting experiments without the need for complex cryogenic thermal control. The fluids, supplied by 3M, have a declared purity level of 99.5%.

In addition, HFEs exhibit low toxicity, are nonflammable and thermally stable, and thus have excellent environmental compatibility. [20]

The properties shown in this thesis are based on the work of Rausch et al. [20]. The properties are shown in the figures below.

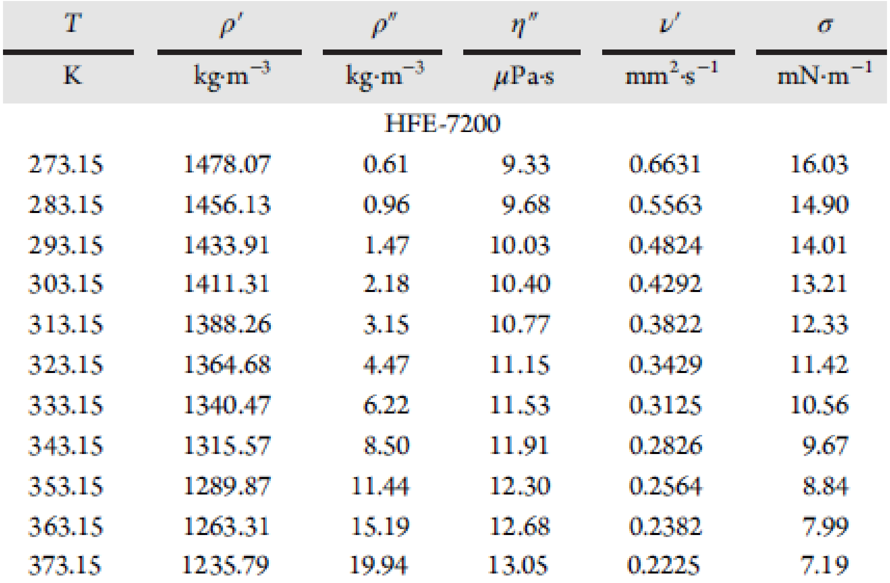

T K	ρ' $kg\cdot m^{-3}$	ρ'' $kg\cdot m^{-3}$	η'' $\mu Pa\cdot s$	ν' $mm^2\cdot s^{-1}$	σ $mN\cdot m^{-1}$
		HFE-7200			
273.15	1478.07	0.61	9.33	0.6631	16.03
283.15	1456.13	0.96	9.68	0.5563	14.90
293.15	1433.91	1.47	10.03	0.4824	14.01
303.15	1411.31	2.18	10.40	0.4292	13.21
313.15	1388.26	3.15	10.77	0.3822	12.33
323.15	1364.68	4.47	11.15	0.3429	11.42
333.15	1340.47	6.22	11.53	0.3125	10.56
343.15	1315.57	8.50	11.91	0.2826	9.67
353.15	1289.87	11.44	12.30	0.2564	8.84
363.15	1263.31	15.19	12.68	0.2382	7.99
373.15	1235.79	19.94	13.05	0.2225	7.19

Figure A.6: Liquid Density ρ', Vapor Density ρ'', Dynamic Viscosity of the Vapor Phase η'', Kinematic Viscosity of the Liquid Phase ν', and Surface Tension σ of HFE7200 for T = (273.15 to 373.15) K at Saturation Conditions

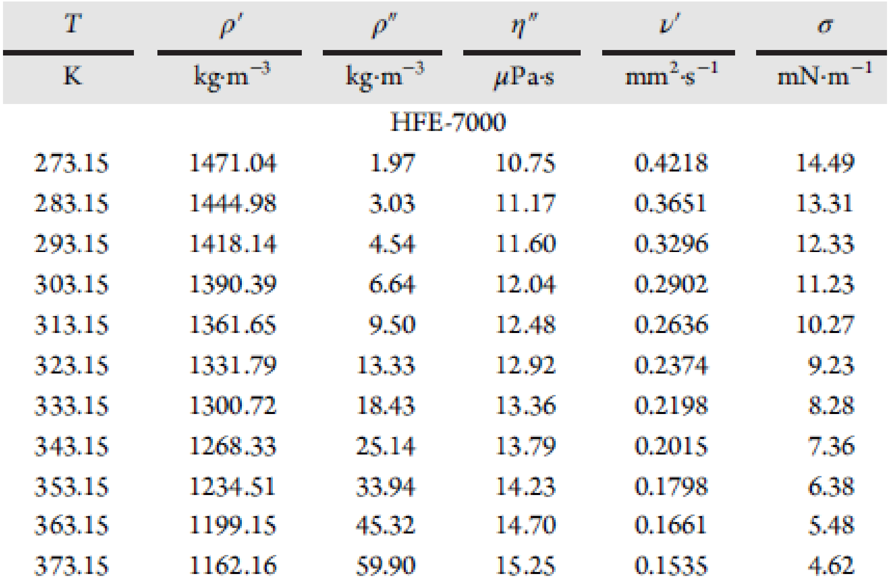

T	ρ'	ρ''	η''	ν'	σ
K	$kg \cdot m^{-3}$	$kg \cdot m^{-3}$	$\mu Pa \cdot s$	$mm^2 \cdot s^{-1}$	$mN \cdot m^{-1}$
HFE-7000					
273.15	1471.04	1.97	10.75	0.4218	14.49
283.15	1444.98	3.03	11.17	0.3651	13.31
293.15	1418.14	4.54	11.60	0.3296	12.33
303.15	1390.39	6.64	12.04	0.2902	11.23
313.15	1361.65	9.50	12.48	0.2636	10.27
323.15	1331.79	13.33	12.92	0.2374	9.23
333.15	1300.72	18.43	13.36	0.2198	8.28
343.15	1268.33	25.14	13.79	0.2015	7.36
353.15	1234.51	33.94	14.23	0.1798	6.38
363.15	1199.15	45.32	14.70	0.1661	5.48
373.15	1162.16	59.90	15.25	0.1535	4.62

Figure A.7: Liquid Density ρ', Vapor Density ρ'', Dynamic Viscosity of the Vapor Phase η'', Kinematic Viscosity of the Liquid Phase ν', and Surface Tension σ of HFE7000 for T = (273.15 to 373.15) K at Saturation Conditions

A.4 Evaporation rate experiment

In this appendix, an estimate of the volumes of the experimental setup is given, and a second approach is used to study the evaporation of HFEs, considering the exposed surface area.

A.4.1 Volume estimation

In this section, we have given the experimental setup's estimated volumes to find the saturation time.

The diagram in Fig. A.8 shows the volumes taken into account for the calculation.

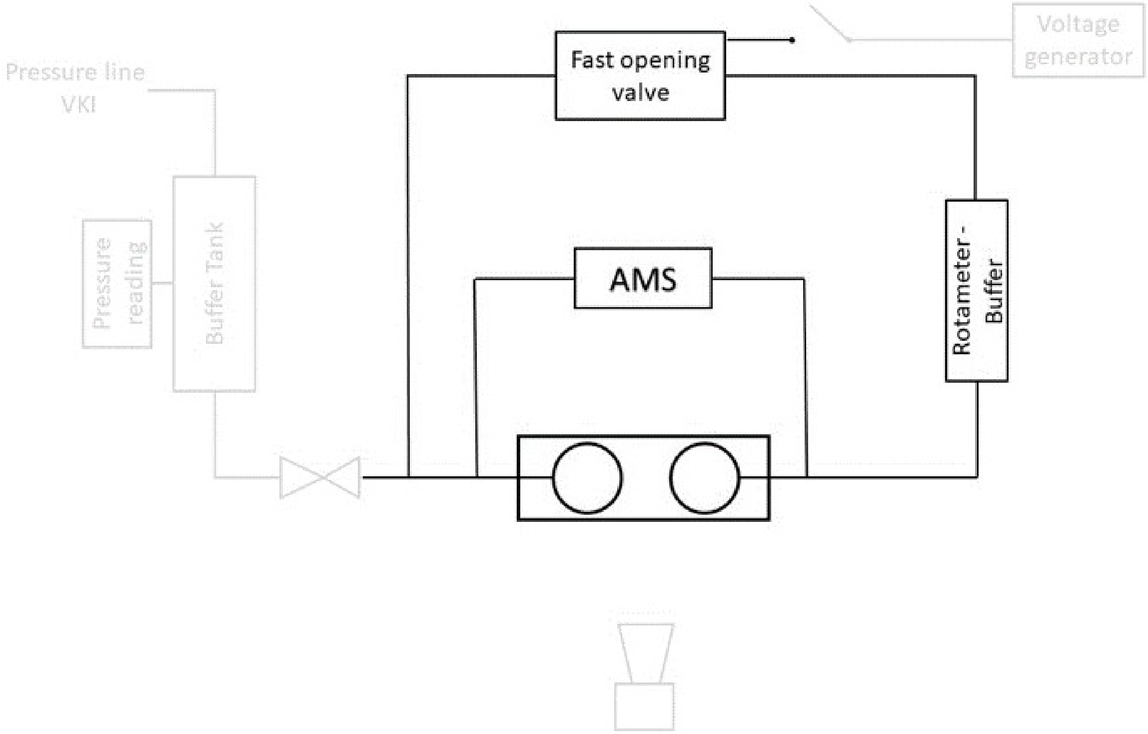

Figure A.8: Volumes included in the estimation

These include the upper part of the empty U-shaped tube, the connections made with pipes with an internal diameter of 5 *mm*, the connections to the AMS with pipes with an internal diameter of 1 *mm*, the Fast Opening Valve (FOV) and the buffer.

We modeled the FOV as a cylinder with an internal diameter of 1 *cm* and height of 10 *cm*, while the volume of the rotameter - buffer is approximated to a cylinder of diameter 5 *cm* and height of 30 *cm*. We considered a length of 40 *cm* of pipes per side and 10 *cm* of pipes for the AMS connection.

- $V_{buffer} = 589.05\ cm^3$
- $V_{pipes} = 15.70\ cm^3$
- $V_{AMS_{pipes}} = 0.15\ cm^3$
- $V_{FOV} = 31.41\ cm^3$

The total volume to be saturated is:

$$V_{setup} = \sum_i V_i = 636.31\ cm^3$$

A.4.2 Treatment with evaporation surface

In this appendix, we examine the evaporation process considering the evaporation area of the HFE droplet, which was omitted earlier for simplicity of discussion. This approach makes it possible to calculate the evaporation rate per unit area so that it can be related to the area exposed to the air inside the U-shaped tube.

In both cases of HFE, the largest drop tested has a radius of 1 cm. Assuming that the radius decreases with rate $\sqrt{t}$, it is possible to see how the area of the droplet exposed to air changes. The Figures below show the function of area reduction.

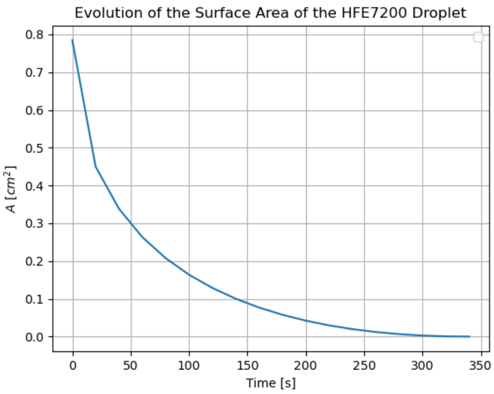

Figure A.9: Area reduction in a HFE7200 droplet

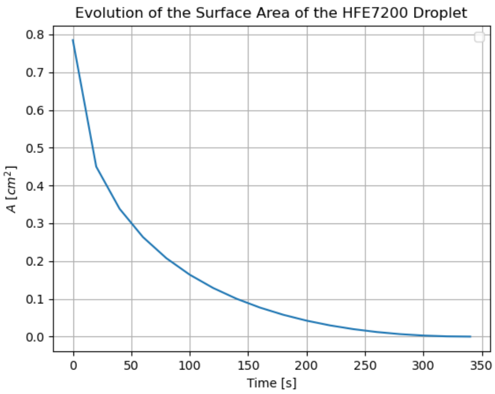

Figure A.10: Area reduction in a HFE7000 droplet

We take as a case study the first tube, with radius 4 mm. It means that the surface is $A = 0.5026\ cm^2$. Analyzing the graph in Fig. A.9 and A.10, the surface A is reached in 17 s in the case of HFE7200 and in 7.6 s in the case of HFE7000.

Figures A.11 and A.12 show the evaporation rate of the HFEs, including the evaporation surface.

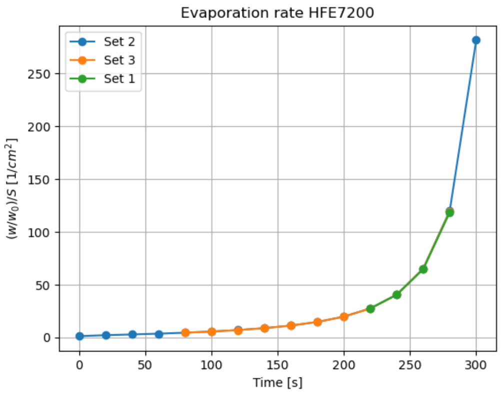

Figure A.11: Evaporation rate of HFE7200 including the surface

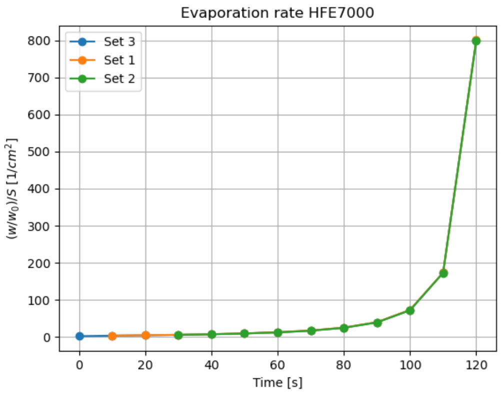

Figure A.12: Evaporation rate of HFE7000 including the surface

It can be seen that the area of interest is the rectilinear part of the graphs, so it is possible to calculate the angular coefficient of the regression line that approximates the experimental data.

In this case, the evaporation rates per unit area are:

- HFE7200: $Evaporation\ rate = 1.66 \cdot 10^{-2}\ g/cm^2/s$
- HFE7000: $Evaporation\ rate = 5.01 \cdot 10^{-2}\ \ g/cm^2/s$

Multiplying by the evaporation surface area in the case of the U-shaped tube of $R = 4\ mm$ gives the evaporation rate expressed as $[g/s]$. Multiplying by the evaporation surface area in the case of the U-shaped tube of $R = 4\ mm$ gives the evaporation rate expressed as $[g/s]$.

- HFE7200: $Evaporation\ rate = 8.34 \cdot 10^{-3}\ g/s$
- HFE7000: $Evaporation\ rate = 2.52 \cdot 10^{-2}\ \ g/s$

Calculating the saturation time for the volume of the setup in the case of the HFE7200, we obtain:

$$t_{sat} = \frac{m_{HFE7200-gas}}{dm/dt}$$

The mass of vapours of HFE7200 in the air is: $m_{HFE7200-gas} = \rho_{HFE7200-gas} \cdot V_{HFE7200-gas} = 0.1236\ g$, thus,

$$t_{sat} = 14.82\ s$$

According to this analysis, the saturation time is shorter than previously calculated. The treatment has many limitations, one of which could be the approximation of the volumes involved and the estimation of the droplet area in the case of the evaporation experiment.

Appendix B

Results

B.1 Fluids Comparison

This section presents a complete comparison of the fluids used in the experiment. Previously, to improve readability, the graphs were divided into two separate graphs.

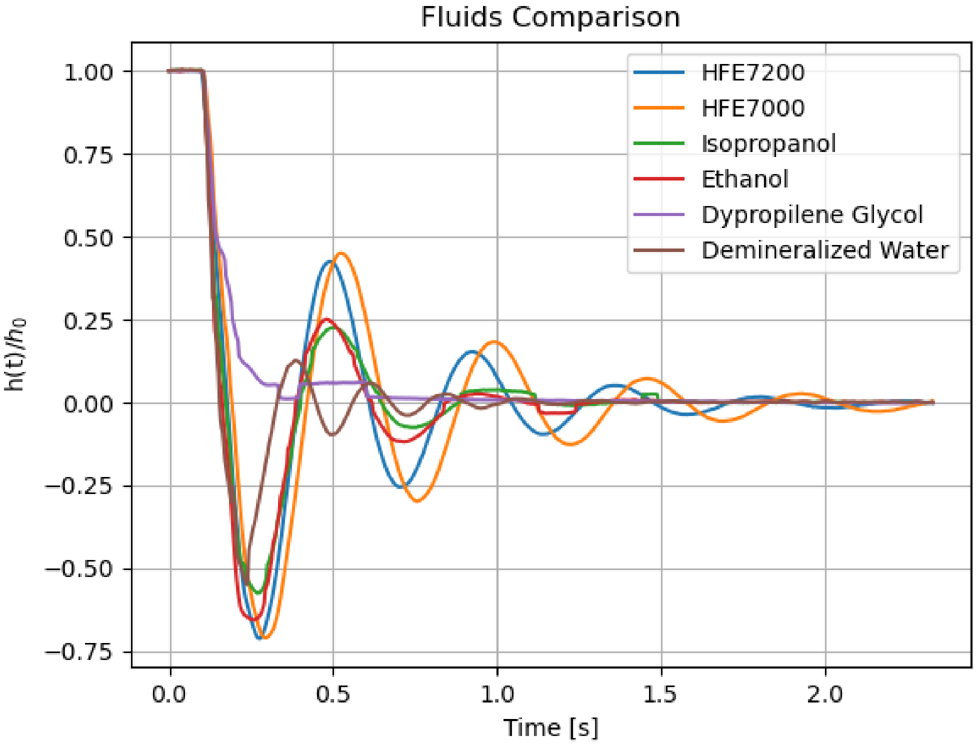

Figure B.1: Interface evolution over time

The next sections show pictures of the experiments with HFEs and demineralized water.

B.1.1 HFE7200 test

Test carried out with HFE7200 with the first tube, $V = 4\ ml$, $\Delta h = 2\ cm$.

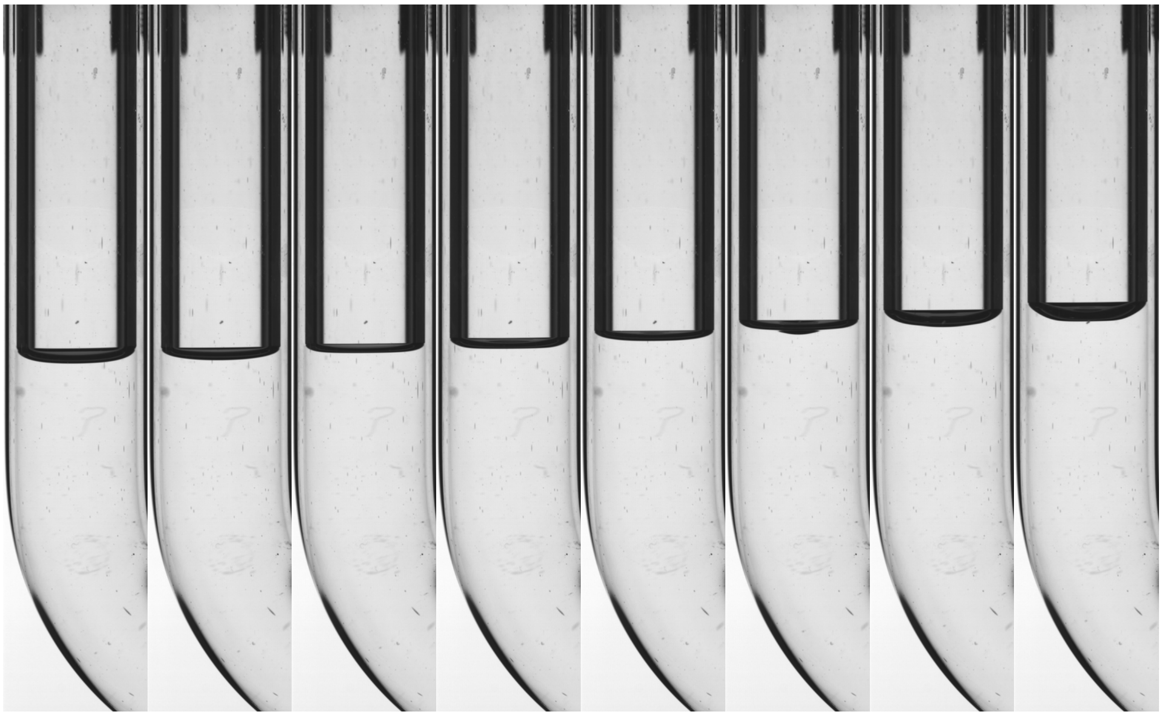

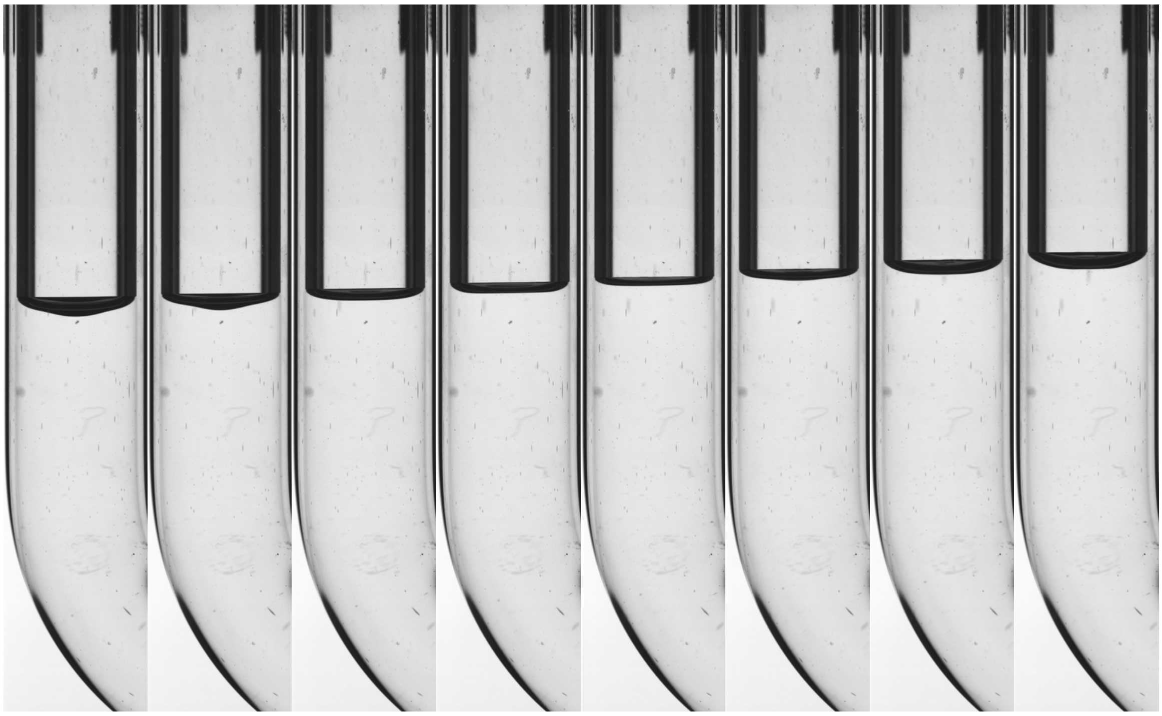

B.2 HFE7000 test

Test carried out with HFE7000 with the first tube, $V = 4\ ml$, $\Delta h = 2\ cm$.

B.3 Demineralized Water test

Test carried out with Demineralized Water with the first tube, $V = 4\ ml$, $\Delta h = 2\ cm$.

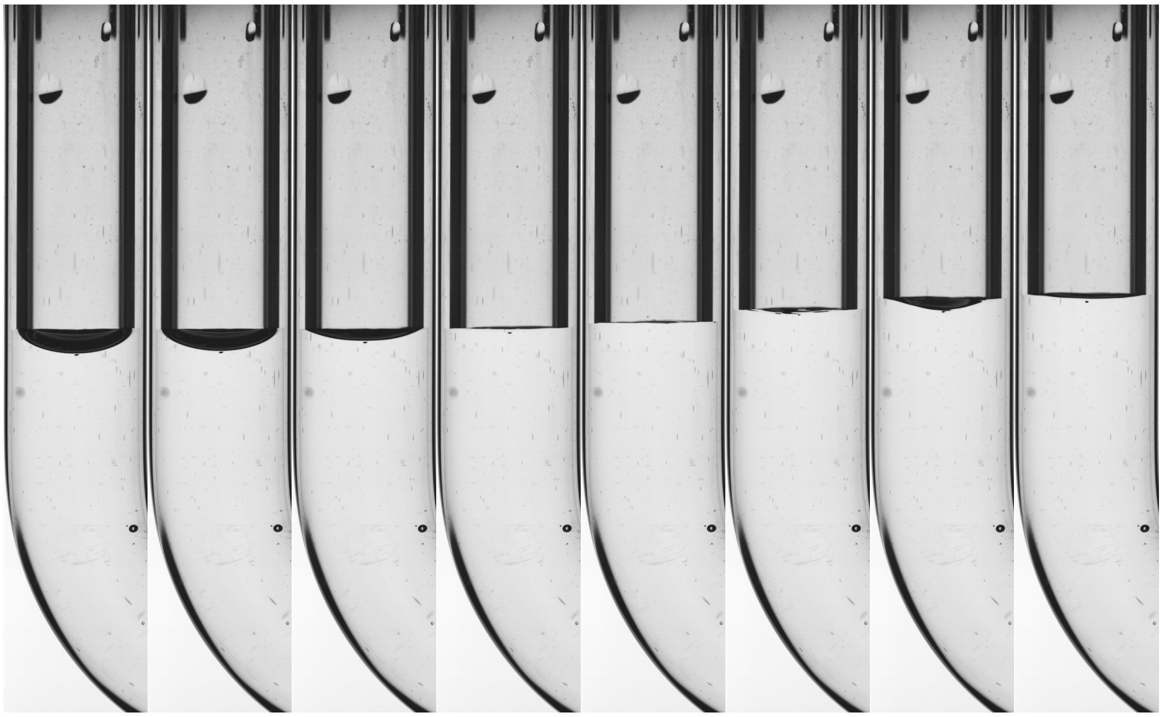

Bibliography

[1] Kun Ma et al. "Visualization of improved sweep with foam in heterogeneous porous media using microfluidics". In: *Soft Matter* 8 (41 2012). In Abstract published on The Royal Society of Chemistry, pp. 10669–10675. DOI: `10.1039/C2SM25833A`.

[2] Ayokunle Olanrewaju et al. "Capillary microfluidics in microchannels: from microfluidic networks to capillaric circuits". eng. In: *Lab on a chip* 18.16 (2018), pp. 2323–2347. ISSN: 1473-0197.

[3] Xiaoyu Ding, Jianhua Liu, and Tequila A. L. Harris. "A review of the operating limits in slot die coating processes". eng. In: *AIChE journal* 62.7 (2016), pp. 2508–2524. ISSN: 0001-1541.

[4] Teruo Fujii. "PDMS-based microfluidic devices for biomedical applications". In: *Microelectronic Engineering* 61-62 (2002). In Abstract, pp. 907–914. ISSN: 0167-9317. DOI: `https://doi.org/10.1016/S0167-9317(02)00494-X`. URL: `https://www.sciencedirect.com/science/article/pii/S016793170200494X`.

[5] Shi Cheng and Zhigang Wu. "Microfluidic electronics". eng. In: *Lab on a chip* 12.16 (2012). In Abstract, pp. 2782–2791. ISSN: 1473-0197.

[6] Yuhan Li et al. "Calculation of Capillary Rise Height of Soils by SWCC Model". eng. In: *Advances in civil engineering* 2018 (2018). In Abstract, pp. 1–10. ISSN: 1687-8086.

[7] Mark M. Weislogela et al. "The capillary flow experiments aboard the International Space Station: Status". In: *Acta Astronautica 65 (2009) 861 – 869* (Apr. 2009). DOI: `https://doi-org.ezproxy.biblio.polito.it/10.1016/j.actaastro.2009.03.008`.

[8] Prof. Dario Pastrone. *Endoreattori Avanzati - A.A. 2022/23 - Propellant Management*.

[9] J.P.B. Vreeburg. *Spacecraft maneuvers and slosh control.* eng. New York, 2005.

[10] Jintao Liu et al. “Experimental investigation of liquid transport in a vane type tank of satellite with microgravity”. eng. In: *Aerospace science and technology* 105 (2020). In Abstract published on ScienceDirect, pp. 106007–. ISSN: 1270-9638.

[11] Jason W. Hartwig. “A Detailed Historical Review of Propellant Management Devices for Low Gravity Propellant Acquisition”. In: *NASA Glenn Research Center, Cleveland, OH, 44135, USA* (July 2016).

[12] J.-C. Fernandez-Toledano et al. “On the cohesion of fluids and their adhesion to solids: Young’s equation at the atomic scale”. In: *Advances in Colloid and Interface Science* 245 (2017), pp. 102–107. ISSN: 0001-8686. DOI: `https://doi.org/10.1016/j.cis.2017.03.006`. URL: `https://www.sciencedirect.com/science/article/pii/S0001868616303244`.

[13] Jonathan M Ludwicki et al. “Is contact-line mobility a material parameter?” eng. In: *NPJ microgravity* 8.1 (2022), pp. 6–6. ISSN: 2373-8065.

[14] Maria Ponomar et al. “Sessile Drop Method: Critical Analysis and Optimization for Measuring the Contact Angle of an Ion-Exchange Membrane Surface”. In: *Membranes 2022, 12(8), 765* (Aug. 2022). DOI: `https://doi.org/10.3390/membranes12080765`.

[15] Jordan G. Petrov and Rossen V. Sedev. “Quasi-static shape of the steady moving meniscus — comparison of the apparent and extrapolated dynamic contact angles”. eng. In: *Colloids and surfaces. A, Physicochemical and engineering aspects* 74.2 (1993), pp. 233–241. ISSN: 0927-7757.

[16] Friedhelm Schönfeld and Steffen Hardt. “Dynamic contact angles in CFD simulations”. eng. In: *Computers & fluids* 38.4 (2009), pp. 757–764. ISSN: 0045-7930.

[17] Takehiro Himeno, Toshinori Watanabe, and Akira Konno. “Numerical Analysis for Propellant Management in Rocket Tanks”. eng. In: *Journal of propulsion and power* 21.1 (2005), pp. 76–86. ISSN: 0748-4658.

[18] S. Afkhami, S. Zaleski, and M. Bussmann. “A mesh-dependent model for applying dynamic contact angles to VOF simulations”. eng. In: *Journal of computational physics* 228.15 (2009), pp. 5370–5389. ISSN: 0021-9991.

[19] D. Fiorini et al. "Effect of inertia on the dynamic contact angle in oscillating menisci". In: *Physics of Fluids* (Oct. 2022). DOI: 10.1063/5.0119863.

[20] Michael H. Rausch et al. "Density, Surface Tension, and Kinematic Viscosity of Hydrofluoroethers HFE-7000, HFE-7100, HFE-7200, HFE-7300, and HFE-7500". In: *Journal of Chemical & Engineering Data* (Nov. 2015). DOI: 10.1021/acs.jced.5b00691.

[21] VKI Faculty. *Measurement Techniques in Fluid Fynamics, An Introduction.* Von Karman Institute for Fluid Dynamics, 2009.

[22] Druck DPI 610/615. *User manual - K0415*. Sensing & Inspection Technologies.

[23] Domenico Fiorini et al. "Dynamic Wetting Experiment with Cryogenic Nitrogen". In: ().

[24] Chanwoo Park Milad Darzi. "Optical distortion correction of a liquid-gas interface and contact angle in cylindrical tubes". In: *Physics of Fluids 29, 052004* (2017). DOI: https://doi.org/10.1063/1.4982902.

[25] Friedhelm Schönfeld and Steffen Hardt. "Support Vector Regression". eng. In: *Computers & fluids* (2015). DOI: DOI:10.1007/978-1-4302-5990-9_4.

[26] Rafael Tadmor. "Open Problems in Wetting Phenomena: Pinning Retention Forces". eng. In: *Langmuir* 37.21 (2021), pp. 6357–6372. ISSN: 0743-7463.

[27] Yi Xia and Paul H. Steen. "Moving contact-line mobility measured". eng. In: *Journal of fluid mechanics* 841 (2018), pp. 767–783. ISSN: 0022-1120.

[28] Domenico Fiorini et al. "Characterization of a capillary-driven flow in microgravity by means of optical technique". eng. In: *Multiphase Science and Technology* (2023). DOI: 10.1615/MultScienTechn.2023047919.

Acknowledgements

I would like to express my sincere gratitude to the Von Karman Institute for the incredible opportunity it has provided me with. I would like to personally thank Professor Miguel Alfonso Mendez, who has been my mentor and guide throughout the journey. His wisdom, expertise, and unwavering support have been instrumental in my success. I am also grateful to Alessia Simonini, who has guided me with care and precision at every step of my journey. Her dedication and competence have significantly contributed to my learning. I cannot forget to mention Domenico Fiorini, who has demonstrated exceptional patience, dedication, and availability. He has played a key role in my progress. Lastly, I would like to extend my immense gratitude to Professor Dario Pastrone from the Politecnico di Torino, my academic home during my university years. Professor Pastrone's close guidance and valuable insights for reflection have enriched my experience and opened new perspectives. I am deeply grateful to all of you for believing in me.